ACS APPLIED NANO MATERIALS

www.acsanm.org Article

Role of ZnO in ZnO Nanoflake/Ti_3C_2 MXene Composites in Photocatalytic and Electrocatalytic Hydrogen Evolution

Bhagirath Saini, Harikrishna K, Devika Laishram, R Krishnapriya, Rahul Singhal, and Rakesh K. Sharma*

Cite This: *ACS Appl. Nano Mater.* 2022, 5, 9319−9333 Read Online

ACCESS | Metrics & More | Article Recommendations | Supporting Information

ABSTRACT: Herein, we report a simple hydrothermal synthesis of ZnO-Ti_3C_2 MXene nanocomposites with a varying wt % of ZnO to exploit the synergistic effect of 2D layer structured Ti_3C_2 and semiconductor ZnO for photocatalysis and electrocatalysis applications. A systematic study on the efficiency of ZnO-Ti_3C_2 nanocomposites toward the degradation of organic pollutants (dyes and pharmaceuticals) and the hydrogen evolution reaction (HER) is demonstrated. Among the developed nanohybrid catalysts, the ZnO-Ti_3C_2 composite with 10 wt % ZnO (MXZnO-10) showed the highest photodegradation efficiency of 76.4% within 10 min of the reaction and 99.2% in 60 min for methylene blue (MB) dye. The synergistic interactions between 2D layered Ti_3C_2 and ZnO improved the lifetime of electrons and holes by reducing the recombination rate. The uncombined electrons and holes facilitated the effective degradation of the MB dye. The ZnO-Ti_3C_2 nanocomposite with 5 wt % ZnO (MXZnO-5) showed excellent HER performance and exhibited an overpotential of 495 mV at 10 mA/cm^2 with a Tafel slope of 108 mV/dec. This work widens the application range of transition metal oxide−MXene composites, providing potential substitute materials for photocatalysis and electrocatalysis applications.

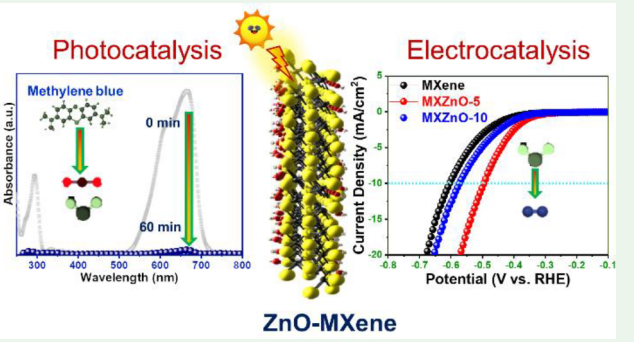

KEYWORDS: *ZnO nanoflakes, MXenes, nanocomposites, photocatalysis, electrocatalysis, hydrogen evolution*

INTRODUCTION

Harnessing a clean, affordable, and inexhaustible source of energy; its storage; and addressing environmental pollution necessitates extensive scientific attention. Currently, the environment pays the price of excessive fossil fuel consumption with a massive 31.5 GT of carbon emissions, which can be curbed by switching to green energy technologies.[1] To meet the worldwide energy demand, "hydrogen" provides an alternative greener fuel option owing to its zero-emission byproducts.[2,3] Another primary concern is the increasing pollution level of water resources due to careless human activities such as the direct dumping of industrial wastes into natural water resources. As numerous dyes are being used in the textiles and paper manufacturing industries, aquatic living beings are facing higher fatality. As a potential solution to many environmental problems, electrocatalysis and photocatalytic degradation of pollutants (dyes, antibiotics, and heavy metals) using nanomaterials are profuse scientific interests to positively impact human health and the environment. As a possible solution, 2-D layered nanomaterials, particularly g-C_3N_4, MoS_2, WS_2, and MXene, are effectively used for photocatalytic and electrocatalytic hydrogen evolution reactions (HER) due to their excellent properties.[4] Among the potential nanomaterials, MXenes find exceptional attention. MXenes have a general formula of $M_{n+1}X_nT_x$, where M represents an early transition metal (Ti, V, Nb, Ta, Cr, Mo, etc.); T refers to the surface terminating functional groups such as oxygen, fluorine, and a hydroxyl group; X represents C or N; and n = 1, 2, or 3. MXene was synthesized in 2011 by the selective etching process of Al from the MAX phase.[5] The precursor MAX phase is treated by a physical and chemical method such as the use of concentrated hydrofluoric acid (HF) to etch out the A layer to achieve the delaminated layer of MXene.[6] These materials exhibit remarkable properties such as metallic conductivity,[7] hydrophilicity,[8] redox activity, good dispersibility, and photochemical stability.[9] Among 100+ MXenes, $Ti_3C_2T_x$ has shown great promise, including in electromagnetic interference shielding,[10] sensors,[11] photocatalytics,[12] and energy storage applications such as supercapacitors and Li-ion batteries.[13]

Interestingly, Ti_3C_2 has a variable bandgap of 0.05 and 0.1 eV owing to the terminal groups −OH and −F, respectively.[14] This narrow bandgap energy is beneficial for producing

Received: April 15, 2022
Accepted: June 30, 2022
Published: July 11, 2022

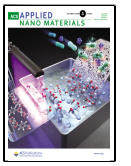

Scheme 1. Synthesis Process of Ti_3C_2 MXene from Ti_3AlC_2

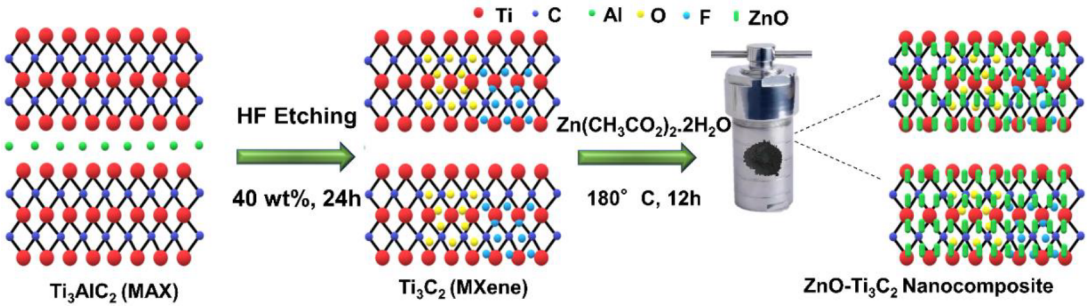

electrons from the semiconductor. Various nanoparticle materials, nanofibers,[15] carbon materials,[16] and carbon nanosheets[17] were incorporated into Ti_3C_2 layers to avoid restacking and improve the surface area to get better catalysts for photocatalysts and electromaterials into catalyst applications. Additionally, incorporating the oxide materials into the Ti_3C_2 could improve the overall catalytic properties and conductivity of Ti_3C_2. Recently, nanostructured transition metal oxides such as Co_3O_4,[18] TiO_2,[19] Fe_2O_3,[20] ZnO,[21] MnO_2,[22] and SnO_2[23] were reported as better photocatalyst and electrocatalyst electrode materials for HER, OER, and supercapacitor applications.

Among these semiconductors, nanostructured ZnO got special consideration for electrocatalytic[21] and dye degradation applications,[24] owing to its low-cost, high surface area, eco-friendliness, and nontoxic nature. Moreover, ZnO can be prepared easily with predefined nanoscale dimensions with good electrochemical properties.[25] ZnO has a direct bandgap of 3.3 eV, suitable for semiconductor-based technological applications and other pharmaceutical, cosmetics, and textile industries.[26] Hybrids of Ti_3C_2 and ZnO nanomaterials could offer high chemical stability, high surface area, electrode−electrolyte interaction, and excellent electromagnetic absorption.[27] Limited examples pertaining to ZnO and Ti_3C_2 combination in photocatalysis have been reported with unconfirmed loading of ZnO and dye mineralization.[28−31]

In this context, we report the synthesis of multilayered 2D ZnO-Ti_3C_2 nanohybrids using Ti_3AlC_2 with 5, 10, and 15 wt % of ZnO (named MXZnO-5, MXZnO-10, and MXZnO-15) for various catalytic applications. A simple one-pot hydrothermal process was used to synthesize a sandwich-like nanoarchitecture in which ZnO nanoparticles are distributed uniformly on the surface and between the MXene layers as shown in Scheme 1. When applied as the photocatalyst, the material exhibited excellent photocatalytic degradation of dyes. The material also showed its potential as active electrode material for HER.

EXPERIMENTAL SECTION

Synthesis of MXene. $Ti_3C_2T_x$ were prepared by the etching of the Al layer from the as-purchased MAX (Ti_3AlC_2) phase precursor. The Ti_3C_2 solution was prepared by immersing slowly 2 g of MAX power in a 40 mL aqueous solution of 40 wt % HF acid in a polypropylene beaker and continuously stirring it at room temperature for 24 h. The resultant solution of Ti_3C_2 was centrifuged at 3500 rpm and washed out several times with the DI water to remove AlF_3 and excess HF acid until the neutral pH of the supernatant was reached. To obtain Ti_3C_2 flakes, the solution was dispersed in 150 mL of water and sonicated for 3 h to increase the interspacing between the layers. Further filtration was carried out followed by drying in a vacuum oven at 80° to obtain multilayered Ti_3C_2.

Synthesis of ZnO-MXene. A one-pot hydrothermal process prepared ZnO-Ti_3C_2. First 200 mg of MXenes was dispersed in water and sonicated for 20 min to obtain a homogeneous suspension. Then, a 0.5 M concentration solution (1) of $Zn(CH_3CO_2)_2{\cdot}2H_2O$ and a 0.25 M concentration solution (2) of NaOH solution were prepared separately. A white suspension was observed during the addition of solution 2 into solution 1 dropwise with continuous stirring. Finally, a white precipitate solution and a Ti_3C_2 solution were added to 33 mL of DI water to make 5, 10, and 15 wt % ZnO into MXene, named MXZnO-5, MXZnO-10, and MXZnO-15, respectively. The product was heated in a hydrothermal autoclave vessel at a 180 °C temperature for 12 h. Finally, the resultant solution was cooled down at room temperature and dried at 60 °C.

MATERIALS

Titanium aluminum carbide powder (Ti_3AlC_2) was purchased from Nanoshel. Hydrofluoric acid (48% to 51%), NaOH, and extra pure zinc acetate dehydrate (98%) were obtained from Across Organics. Methylene blue was purchased from SRL, and cresol red was purchased from Himedia. p-Benzoquinone, triethanolamine, *tert*-butanol, methyl orange, ibuprofen, and ciprofloxacin were purchased from Sigma-Aldrich. All of the reagents were used intrinsically without further purification, and deionized water was used for the synthesis process.

Dye Degradation Test. The catalytical degradation performance of Ti_3C_2 and ZnO-Ti_3C_2 nanocomposites was evaluated with organic pollutants, including dyes and drugs. Here, different wt % ZnO-Ti_3C_2 catalysts were used for the degradation experiment. In contrast, methylene blue was used as a main probing dye, and the best catalyst was applied for other organic pollutants like MO, CR, IBP, and CIP. All of the experiments were carried out at pH 7. Afterward, the pH of the solution was maintained at around 3.5 and 10 using HCl and NaOH for all of the experiments to check the effect of pH on MB photodegradation. The resultant solution was exposed to 1 sun intensity in a solar simulator, and the catalyst-dye solution was removed in a certain time interval. After centrifugation of the collected sample solution, the supernatant solution was used to measure UV−visible absorption and real-time MB concentration. The degradation efficiency of samples was calculated using the formula $C_0 - C/C_0 \times 100$, where C is the concertation of MB (dye solution) at a different time interval and C_0 is the initial concentration at $t = 0$.

Electrochemical Measurements. A CHI660E-CH Instruments workstation was used to study the specimens at room temperature with a standard three-electrode system. All of the electrochemical measurements for HER were performed in three-electrode cells with a 0.5 M H_2SO_4 aqueous electrolyte. Electrochemical measurements were executed with respect to 3 M Ag/AgCl as a reference electrode, while a glassy carbon electrode (d = 3 mm) coated with the active materials as a working electrode and platinum wire electrode as the counter electrode. Leaner sweep voltammetry (LSV) measurements were tested at a scan rate of 10 mV s^{-1} with internal resistance (iR) compensation. The double-layer capacitance of the samples (C_{dl}) was determined in the nonfaradaic region (0.213 V vs RHE) by measuring capacitive currents at different scan rates. The cycling stability test was performed by long-term chronopotentiometry for 10 h. Electro-

https://doi.org/10.1021/acsanm.2c01639
ACS Appl. Nano Mater. 2022, 5, 9319−9333

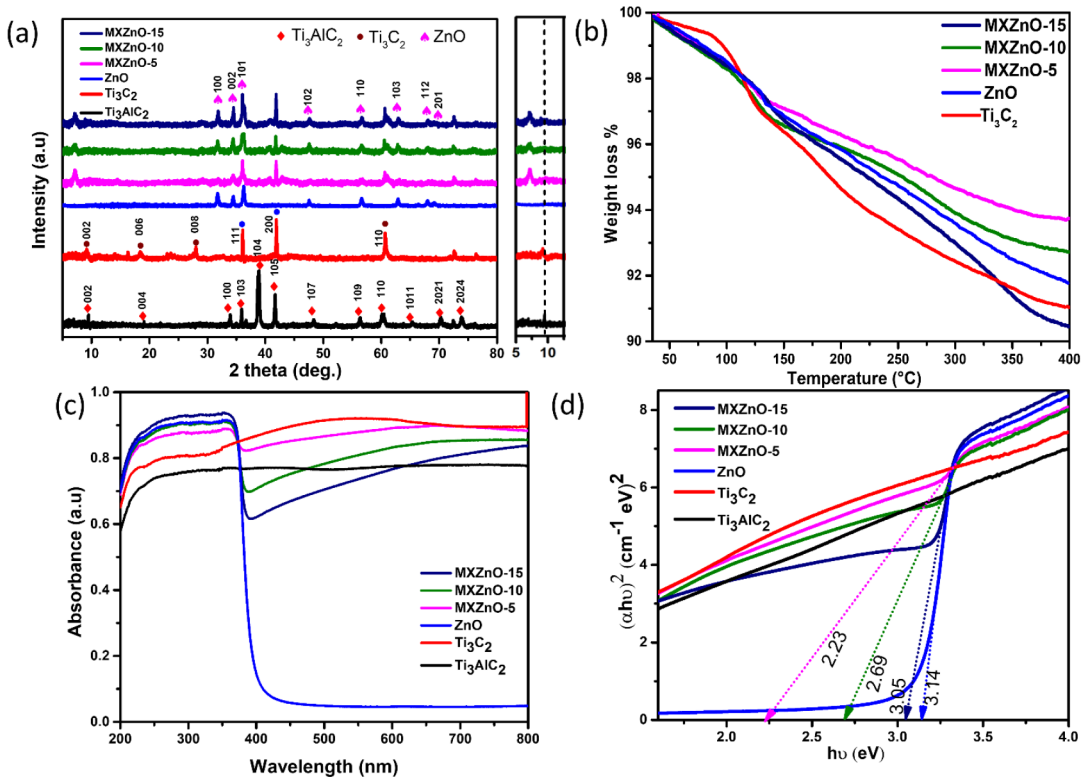

Figure 1. (a) XRD patterns of the Ti_3AlC_2, Ti_3C_2, and ZnO-Ti_3C_2 nanocomposites. (b) TGA curves of the Ti_3C_2, ZnO, and ZnO-Ti_3C_2 nanocomposites. (c) The UV−vis DRS of an as-prepared catalyst and (d) corresponding Tauc plots.

chemical impedance spectroscopy (EIS) studies were conducted in the frequency range between 1×10^6 and 0.1 Hz.

Scavenging Test. The involvement of the primary reactive species (radicals, electrons, and holes) was investigated utilizing several scavenger molecules to determine the mechanism of the photocatalytic activity of ZnO-Ti_3C_2 nanocomposites. Initially, three types of capture scavengers were chosen: triethanolamine (EDTA, an h^+ scavenger), *tert*-butanol (IPA, an OH* scavenger), and p-benzoquinone, (p-BQ, an O^{2-} scavenger) to detect the main reactive species for dye degradation experiments. Three milliliters of each scavenger (0.02 M) is typically dispersed in reaction solutions containing the ZnO-Ti_3C_2 photocatalyst and MB solution, and then it is exposed to light for 60 min.

Preparation of Working Electrodes. The working electrodes were prepared by adding electroactive materials in a 1 mL solution containing 50 μL of Nafion and a mixture of ethanol and DI H_2O (1:1) followed by sonication for 20 min to get a homogeneous solution. Afterward, the materials were dropped and cast onto the glassy carbon electrode to get a 0.15 mg/cm^2 mass loading. Further, the electrode was dried at room temperature to study the electrochemical activity of HER.

CHARACTERIZATION

The synthesized ZnO-Ti_3C_2 composites were analyzed by X-ray diffraction (XRD) techniques using a D8 Advance X-ray diffractometer (Bruker, U.S.A.), with Cu Ka radiation (λ = 1.54 Å) at an accelerating voltage of 45 kV and tube current of 40 mA to scan the diffraction angle range of 5 to 80°. The phase identification was carried out using standard patterns reported in the International Centre for Diffraction Data (ICDD) database. A Brunauer−Emmet−Teller (BET) method for N_2 adsorption−desorption was performed to measure the specific surface area to understand the effect in photocatalysis and electrocatalysis applications using the Quantachrome Autosorb iQ3 instrument. The as-synthesized ZnO Ti_3C_2 composites were subjected to degassing for 120 min at 150 °C to remove all of the impurities from the layers. The surface composition and chemical states were determined with an Omicron Nanotechnology (Oxford Instruments) X-ray photoelectron spectroscope (XPS) instrument with monochromatic Al Kα radiation, and the obtained spectra were fitted using a Gaussian function. The peak correction was done with reference to the standard carbon 1s peak obtained at 284.1 eV for Ti (4f), Zn (3f), and O (1s). Thermogravimetric (TGA) analysis was carried out on a simultaneous thermal analyzer (STA) from PerkinElmer at 2.5 bar of gas pressure from room temperature to 450 °C with a heating rate of 10 °C/min under a N_2 atmosphere. The high-performance liquid chromatography 515 pump was equipped using a Waters 2489 system and C18 column (250 mm × 4.6 mm, 5 μm) system with a mobile phase of 60:40 acetonitrile−water at a 1 mL min^{-1} flow rate. The pH of the electrode solution and dye solution was measured using Oakton PH 2700. The surface morphology and component distribution were obtained through scanning electron microscopy techniques (EVO 18 Zeiss) at an accelerating voltage of 20 kV and atomic force microscopy (XE-70, Park System). The electrocatalyst performances and electrochemical impedance spectroscopy (EIS) were measured using a CHI660E-CH Instruments Inc. electrochemical workstation. A PET Photo Emission Tech SS50AAA solar simulator was used as a light source to get one sun irradiation for dye degradation experiments.

RESULTS AND DISCUSSION

Figure 1a represents the XRD patterns of Ti_3AlC_2, Ti_3C_2, pristine ZnO and ZnO-Ti_3C_2 composites with different wt % of ZnO NPs. The (002) peak of Ti_3C_2 shifted toward the lower angle, confirming the successful formation of Ti_3C_2 from

https://doi.org/10.1021/acsanm.2c01639
ACS Appl. Nano Mater. 2022, 5, 9319−9333

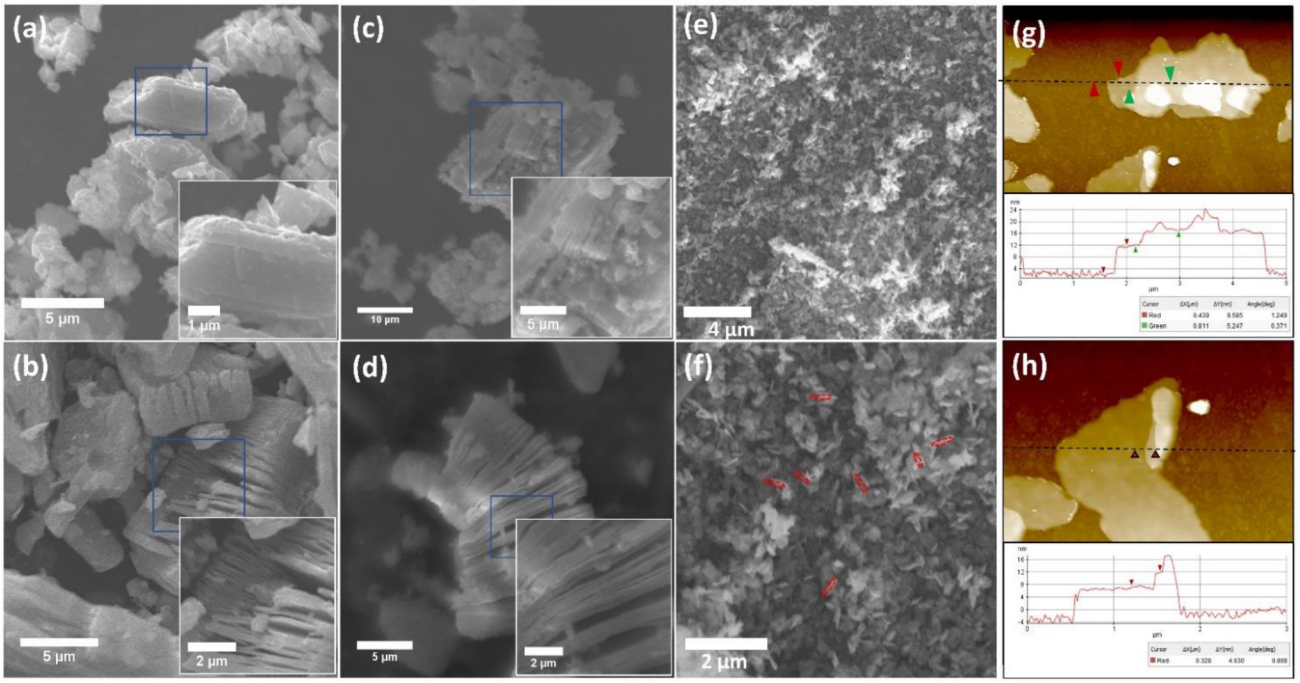

Figure 2. Morphological and structural observation of catalysts: (a) SEM images of Ti_3AlC_2, (b) Ti_3C_2, (c) MXZnO-15, and (d) MXZnO-5 nanocomposites and (e and f) pristine ZnO nanoflakes. Inset images are corresponding large magnification SEM images. Atomic force microscopy (AFM) of (g and h) delaminated Ti_3C_2 MXene and corresponding height profiles.

the Ti_3AlC_2.[5] The bonding between the layers is decreased. The increase of the *c* parameter after HF acid treatment (24 h) is due to selective etching of the Al layer from Ti_3AlC_2.[32] Well-defined diffraction peaks were observed at 2Θ values of 9.4°, 19.0°, 34.0°, 36.7°, 38.8°, 41.7°, 48.4°, 56.4°, 60.2°, 65.4°, 70.3°, and 74.0°, which were indexed to the (002), (004), (100), (103), (104), (105), (107), (109), (110), (1011), (2021), and (2024) planes, respectively, according to the standard JCPDS card number 52-0875 for Ti_3AlC_2. The highly intense peak at 2Θ = 38.8° was not observed in Ti_3C_2, indicating successful removal of the Al layer. The diffraction peaks of Ti_3C_2 can be indexed to (002), (006), (008), and (110) with some impurity peaks of the TiC and TiO_2. These additional peaks are obtained from the precursor and oxidation of the Ti_3C_2 MXene during the etching processes.[33] ZnO-Ti_3C_2 nanocomposites were synthesized using varying wt % of ZnO, in which maximum diffraction intensities were observed in the case of the MXZnO-15 sample (Figure1a). In the XRD pattern of ZnO-Ti_3C_2 composites, ZnO peaks were observed at 2Θ values of 31.5°, 34.3°, 36.2°, 47.6°, 56.6°, 62.9°, 67.9°, and 69.4°, which can be assigned to the (100), (002), (101), (102), (110), (103), (112), and (201) planes of wurtzite ZnO. These peaks are matched with the standard JCPDS card number 00-036-1451 for ZnO. The microstrain values obtained after incorporating ZnO into pristine MXene are given in Table S1. MXene showed a microstrain of 24.67, which increases up to 37.05, indicating the successful incorporation of ZnO. This suggests that the ZnO was successfully grown on the Ti_3C_2 surface. Figure 1b shows the TGA curve of all of the prepared ZnO-Ti_3C_2 with different wt % of ZnO under a nitrogen atmosphere between room temperature and 450 °C. The weight of Ti_3C_2 decreased drastically between 85 and 170 °C. In contrast, the TGA curve of the ZnO-Ti_3C_2 composites shows the weight loss from room temperature to 200 °C owing to removal of the surface-bonded group of −F, −OH, −O, and H_2O. Pristine ZnO shows higher stability compared to Ti_3C_2 and MXZnO-15. It can be observed from the TGA results that MXZnO-5 and MXZnO-10 have less mass percent degradation than the Ti_3C_2 and MXZnO-15. Additionally, MXZnO-5 shows the highest thermal stability and char residues. After incorporating a higher ZnO percentage, MXZnO-15 composition becomes less thermally stable. Diffuse reflectance UV−vis spectroscopy is an essential technique to understand the photocatalytic activity of ZnO incorporated Ti_3C_2. Figure 1c shows the UV−vis absorbance spectra of MXZnO-5, MXZnO-10, MXZnO-15, ZnO, Ti_3C_2, and Ti_3AlC_2. All of the samples displayed absorbance spectra ranging from 200 to 800 nm. Ti_3AlC_2 shows a straight line without any absorption edge, but the Ti_3C_2 showed the absorption edge at 520 nm, indicating the oxidation process happened in a small portion of Ti_3C_2 to TiO_2.[34] ZnO-Ti_3C_2 composites display the absorption edge at 357 nm, which shows the incorporation of ZnO particles. The bandgaps of all samples were estimated via Tauc plot, following the theory of Kubelka and Munk[35] and the following equation.

$$(\alpha h\nu)^2 = A(h\nu - \mathrm{Eg})$$

where α, h, ν, A, and Eg represent the absorption coefficient, Planck's constant, light frequency, direct transition constant, and bandgap, respectively. The bandgap of MXZnO-5, MXZnO-10, MXZnO-15, and ZnO were determined through the Tauc plot as 2.23, 2.69, 3.05, and 3.14 eV, respectively, as shown in Figure 1d. The bandgap is drastically decreased in the case of ZnO-Ti_3C_2 composites compared to ZnO, which can be attributed to the presence of metallic Ti_3C_2.[36] Furthermore, the bandgap decreased from 3.14 to 2.23 due to the higher doping amount of metallic Ti_3C_2 and can be due to the formation of more oxygen vacancies.[37] Because of the lower bandgap of 2.69 eV, MXZnO-10 is expected to exhibit better photocatalytic degradation than pristine ZnO. The

https://doi.org/10.1021/acsanm.2c01639
ACS Appl. Nano Mater. 2022, 5, 9319−9333

MXZnO-5 composition has the lowest bandgap and surface area compared to other ZnO-Ti_3C_2 compositions, affecting interfacial interaction between Ti_3C_2 and ZnO. Figure 2 shows high magnification scanning electron microscopy (SEM), which captures a clear morphology of the as-synthesized ZnO-Ti_3C_2 multilayer composites. Figure 2a,b represent the SEM images of the Ti_3AlC_2 phase and Ti_3C_2, respectively. The HF treatment results in a specific stack of individual sheets of multilayer Ti_3C_2 after the etching of Al from the Ti_3AlC_2. It can be noticed from the inset magnified SEM image in Figure 2a,b that the average Ti_3AlC_2 grain is below 20 μm, and in the exfoliated Ti_3C_2, the layer thickness varies between 2 and 10 nm. As confirmed by BET analysis, Figure 2c,d denote the ZnO anchored Ti_3C_2, showing an increased surface area. Synthesis of pristine ZnO shows the highly dense and uniform rice-like nanoflake structure as seen in Figure 2e,f. AFM of Ti_3C_2 was taken after the etching, washing, sonication, and centrifugation from Ti_3AlC_2. The as-synthesized Ti_3C_2 shows a single, double, or multilayer. The thickness of the layer was around 4.6 and 9.5 nm, which can be due to the single- and double-layered Ti_3C_2 as shown in Figure 2 g and h. The energy-dispersive X-ray spectroscopy technique was further conducted on the colored square district labeled to study the distribution of Ti, Zn, C, O, F, and Al in the multilayer ZnO-Ti_3C_2 composite as shown in Figure S1. The less intense Al peaks denote Al's replacement from Ti_3AlC_2 with a surface group like O and OH. The O element was observed in EDX owing to the formation of ZnO, TiO_2, and a surface termination group with F, OH, and O.

The surface morphology and component distribution were further characterized by TEM. In the ZnO-Ti_3C_2 nanocomposite in Figure 3a, ZnO exhibits a rod and rice-like structure over the MXene sheets. The elemental mapping further reveals the distribution, and the SEM image in Figure 3b shows the HRTEM image of the ZnO-Ti_3C_2 nanocomposite, which shows the lattice fringes of the ZnO. In Figure 3d, the measured interplanar distance of 0.246 nm corresponds to the (101) plane of ZnO, which is identical to the value calculated from the standard XRD JCPDS card No 00-036-1451 of ZnO. The selected area electron diffraction SAED pattern in Figure 3c shows a combination of diffraction rings of ZnO (201, 210, and 302) and hexagonal diffraction spots of Ti_3C_2. The same types of SAED patterns have been reported previously for ZnO-Ti_3C_2 and other Ti_3C_2 composites.[38,39]

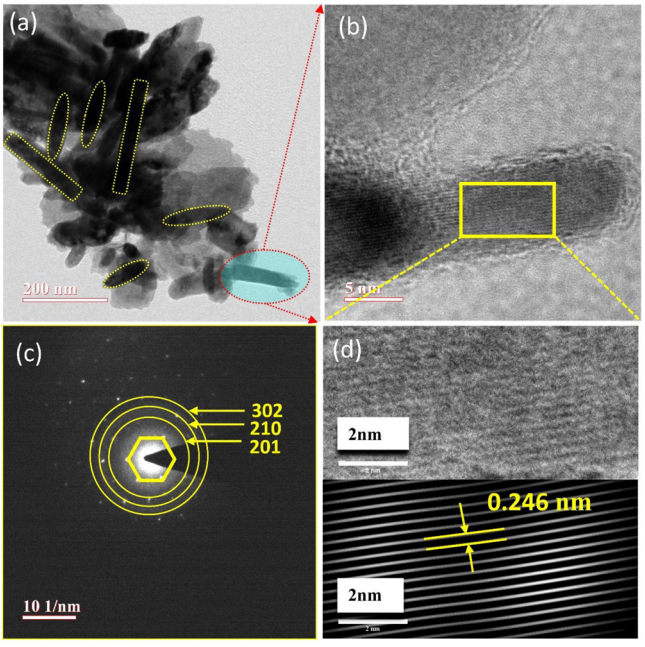

Figure 3. (a and b) Low and high magnification TEM images, (c) SAED patterns (d), inversed fast Fourier transform (IFFT) of a prepared MXZnO-15 catalyst.

The layered structure of MXene can be observed in Figure S2a, demonstrating the removal of the Al layer from Ti_3AlC_2. Figure S2b exhibits a lattice spacing of ~0.98 nm due to the etching process corresponding to (002), which is further confirmed by the XRD, located at $2\Theta = 9.17$. Figure S2c and f represent the SAED pattern of Ti_3C_2, and Ti_3AlC_2, respectively. The symmetrical hexagonal pattern seen in the SAED patterns of the ZnO-Ti_3C_2, and Ti_3AlC_2 indicates that the hexagonal crystal structure is maintained after the HF treatment and hydrothermal reaction.

Figure 4a shows the pore size distribution, demonstrating mesopore voids ranging from 10 to 50 Å. The previous studies revealed that MXene has a pore distribution ranging from 4 to 100 nm, which mainly depends upon the formation of TiO_2 between the space of layers.[40] Figure 4b and c show the N_2 adsorption/desorption isotherms and multipoint BET of the Ti_3C_2 and the ZnO-Ti_3C_2 nanocomposites. Type IV isotherms with apparent hysteresis loops are seen in pristine Ti_3C_2 and ZnO-Ti_3C_2 nanocomposites, caused by mesoporous voids between the Ti_3C_2 layers. As can be observed, all samples have volumes ranging from 0.0068 to 0.0321 cc/g. The average BJH pore diameter is centered at 40.2−46.62 Å, as shown in Table S2. The BET surface area and pore volume increase with the increasing metal oxide into MXene materials. The surface area and pore size distribution of pristine ZnO were analyzed and are given in Figure S4. The surface area of pristine ZnO is 22.47 m^2/g, which is much higher than MXene (6.55 m^2/g). When ZnO is incorporated into the layered MXene, ZnO goes in between the layer of MXene, which increases the interlayer spacing and provides more surface area for the composite. The average pore diameter increased with the ZnO incorporation and then decreased further. It can be inferred that the mesoporosity can provide a way for loading larger amounts of guest molecules, and the material can boost photocatalytic and electrocatalytic performance. The specific surface area obtained from the BET method for Ti_3C_2, MXZnO-5, MXZnO-10, and MXZnO-15 is 6.55, 13.06, 25.58, and 31.79 m^2/g, respectively. All of the ZnO-Ti_3C_2 composite shows a higher surface area compared to pure Ti_3C_2. The enhancement in the surface area is due to the formation of ZnO particles on the Ti_3C_2 layer and increased interlayer spacing between the Ti_3C_2 layers. The higher surface area of ZnO-Ti_3C_2 was expected to improve the performances of photocatalysis and electrocatalysis, due to the greater surface interaction between the catalysis and dye molecules or electrolyte solution. Figure 4d shows the Raman spectra of Ti_3C_2 and ZnO-Ti_3C_2 nanocomposites in the 150−3500 cm^{-1} region. Compared to the pristine Ti_3C_2 MXenes, the Raman peaks of ZnO-Ti_3C_2 nanocomposites indicate the successful incorporation of ZnO with MXene (inset image Figure 4d). The peaks around 267 cm^{-1}, 430 cm^{-1}, and 607 cm^{-1} can be ascribed to the Eg(1), A1g and B1g(2), and Eg(2) vibration modes of C and O bonds and Ti−C vibrations, respectively.[38] The Raman peaks at 164 cm^{-1}, 400 cm^{-1}, and 628 cm^{-1} correspond to TiO_2 vibrational modes.[41,42] These

https://doi.org/10.1021/acsanm.2c01639
ACS Appl. Nano Mater. 2022, 5, 9319−9333

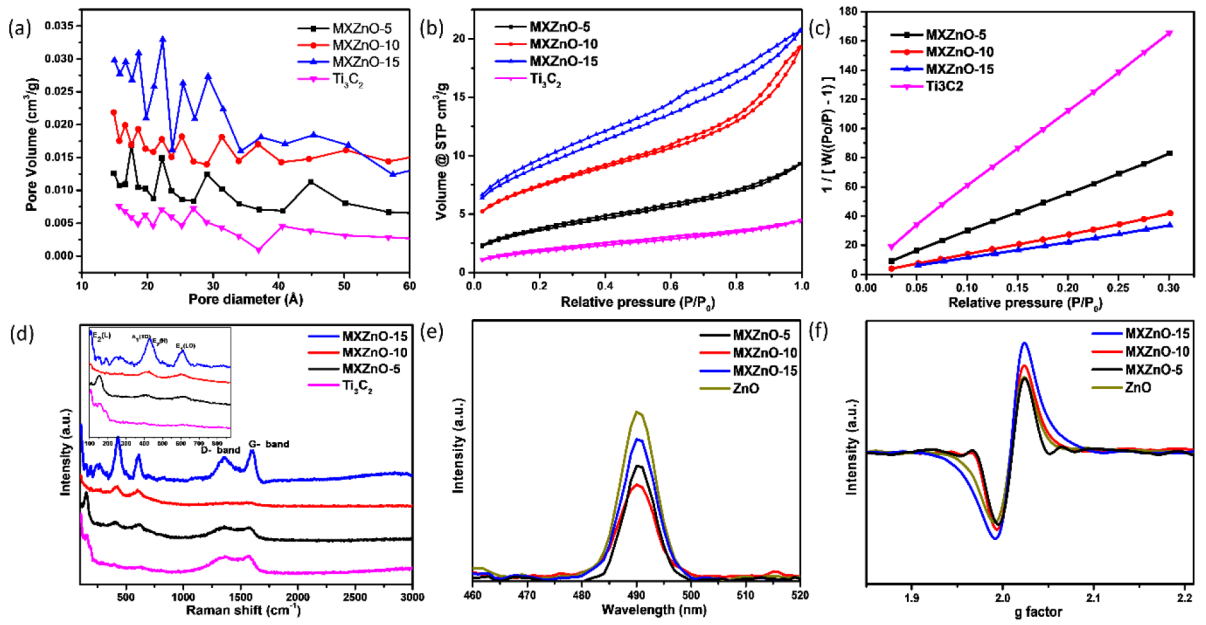

Figure 4. (a) Pore size distribution, (b) nitrogen absorption isotherm, and (c) multipoint BET plots of Ti_3C_2 and ZnO-Ti_3C_2 nanocomposite. (d) Raman spectra of Ti_3C_2 and ZnO-Ti_3C_2 nanocomposite. (e) Photoluminescence spectra and (f) electron paramagnetic resonance spectra of pristine ZnO and ZnO-Ti_3C_2 nanocomposites.

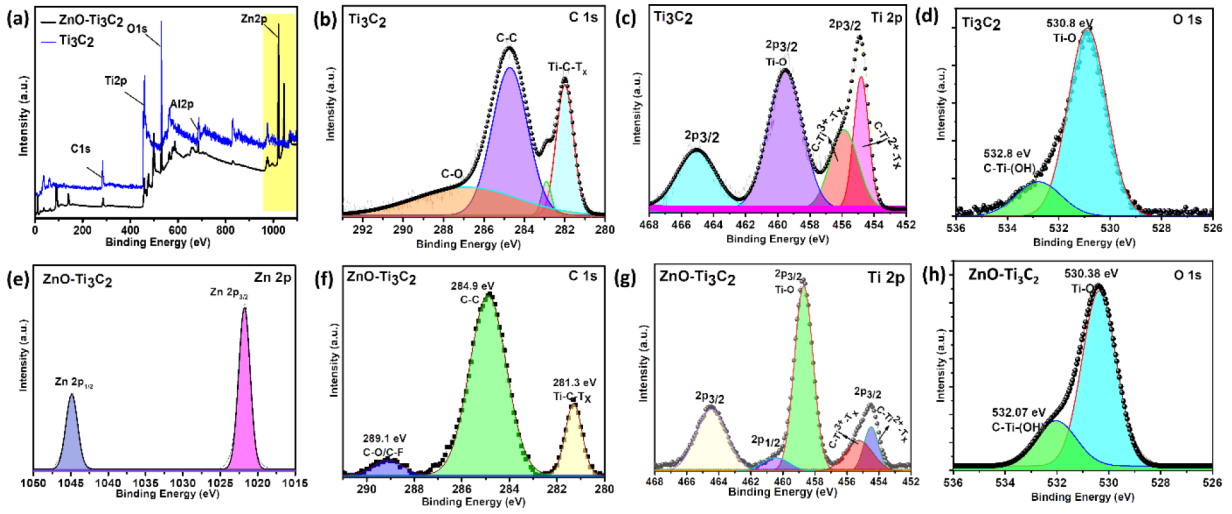

Figure 5. XPS spectra of as-prepared catalyst: (a) survey spectra of Ti_3C_2 MXene and the ZnO-Ti_3C_2 nanocomposite. (b) High-resolution spectra of C 1s, (c) Ti 2p, and (d) O 1s regions for Ti_3C_2 MXene. High-resolution spectra of (e) Zn 2p, (f) C 1s, (g) Ti 2p, and (h) O 1s regions for the ZnO-Ti_3C_2 nanocomposite (MXZnO-10).

results further demonstrate the formation of TiO_2 after the oxidization treatment of Ti_3C_2 MXene shown in XRD. The two broad peaks at 1370 and 1575 cm^{-1} are represented by the D and G modes of graphitic carbon. The increased intensities of D and G bands in the ZnO-Ti_3C_2 nanocomposites indicate the formation of carbon as observed in the XPS plot of the C atom at 284.9 eV. Furthermore, the low intensity of Raman peaks indicates the amorphous carbon content and insufficient oxygen during the process. Figure 4e shows the PL spectra of the ZnO nanostructure and ZnO-Ti_3C_2 composites. Lower PL intensity is associated with a lower electron−hole recombination rate and vice versa, which leads to improved photocatalytic efficacy.[43] The emission peak of pristine ZnO and ZnO-Ti_3C_2 composites was observed with a green emission band around 500 nm, which is commonly attributed to energy level defects in hybrid composites related to singly ionized oxygen vacancy. The PL intensities of all nanohybrid structures are significantly lower than pure ZnO, owing to the effective separation of electron and hole pairs via the Schottky junction. The PL intensity of MXZnO-10 is the lowest compared to other composites, indicating the highest inhibition for electron−hole recombination, hence the higher carrier lifetime. On the basis of these findings, hybrid structures are projected to outperform pristine ZnO in photocatalytic activity. Electron paramagnetic resonance (EPR) spectra were used to investigate the catalyst's oxygen vacancies (Figure 4f). In contrast to other ZnO-Ti_3C_2 composites, the ZnO showed a poor EPR signal. The ZnO and ZnO-Ti_3C_2 nanocomposites showed a signal with a G factor of 2.008, which was persistent with the e^- captured on the oxygen and carbon vacancy

https://doi.org/10.1021/acsanm.2c01639
ACS Appl. Nano Mater. 2022, 5, 9319−9333

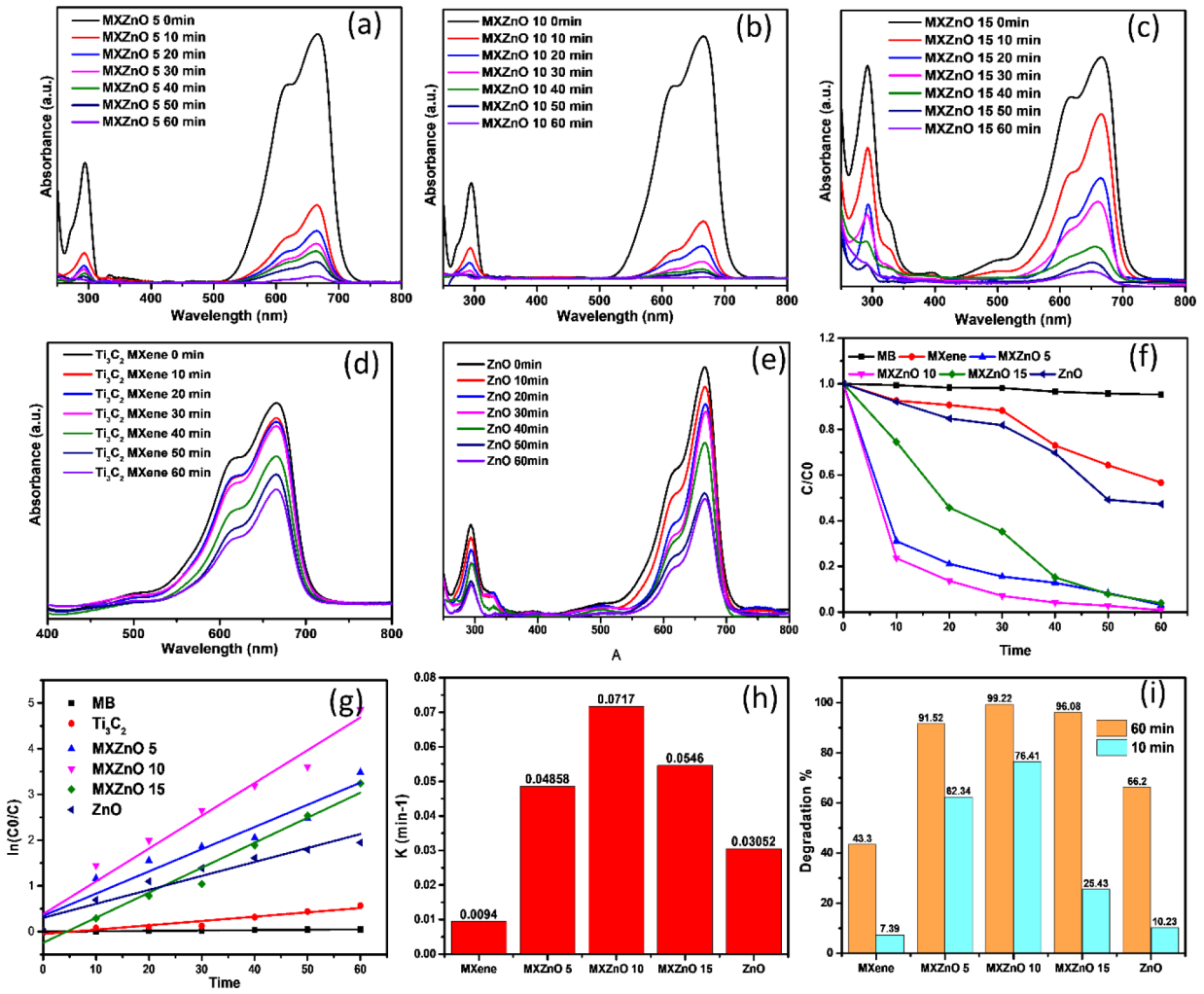

Figure 6. Absorption spectra showing time evolution of the photocatalytic degradation of MB over (a) MXZnO-5, (b) MXZnO-10, (c) MXZnO-15, (d) pristine Ti_3C_2 MXene, and (e) pristine ZnO. (f and g) The variation of photocatalytic degradation of MB dye over Ti_3C_2 MXene, pristine ZnO and ZnO-Ti_3C_2 nanocomposites with a time of irradiations. (h) The rate constant and (i) degradation percentage of MB at 10 and 60 min with Ti_3C_2 MXene, pristine ZnO and ZnO-Ti_3C_2 nanocomposites.

sites.[44,45] ZnO in the synthesis process might have some defect sites leading to the creation of oxygen vacant sites, as observed from the EPR spectra. Meanwhile, in the doped MXenes, ZnO and various terminal Ti sites induce redox activity to create defect sites leading to oxygen vacancies. The formation of increased oxygen vacancies with increased ZnO doping in MXene can be observed from the EPR spectra, where the signal intensity increases with increasing doping concentration. This fact can be corroborated with the XPS result where the doped MXene showed an increase in the oxygen vacancies. The formation of the oxygen vacancy in the composite can also be induced during the oxidation of the MXene into TiO_2. This oxygen vacancy may be due to the defects obtained in the TiO_2 lattice or leaving a surface group like −O or −OH. Some of the previous literature has reported that oxygen vacancies were created in the TiO_2 crystal lattice obtained during the HF etching process.[46,47] Furthermore, an oxygen vacancy signal was observed on MXZnO-10 nanocomposites, suggesting that composites had a higher concentration for better photocatalyst activity.

The surface chemical and electronic state of the ZnO-Ti_3C_2 composite were investigated in detail using XPS analysis for the F 1s, O 1s, C 1s, Ti 2p, Al 2p, and Zn 2p; the results are shown in Figure 5. Figure 5a shows the survey spectrum of the MXene and MXZnO-10 catalyst, indicating the presence of Ti 2p, C 1s, F 1s, Zn 2p, and O 2p. Figure 5b−h show the various high-resolution spectra of individual elements. A small quantity of Al in XPS indicates the residue derived due to the lack of complete etching of Ti_3C_2. This shows that the coexistence of the main surface functional groups like oxide (−O−), hydroxyl (−OH), and −F in XPS can be due to the possible surface termination group of $Ti_3C_2F_2$. The presence of O is due to the surface termination of $Ti_3C_2(OH)_2$.[48] The XPS results confirm the presence of oxide and hydroxyl groups on the surface of MXZnO-10, providing a channel for redox reaction on the surface of the materials, which can help in efficient photocatalytic degradation. Figure 5f shows the C 1s XPS spectra, fitted using three main components at 281.30, 284.91, and 289.11 eV, which may originate from Ti−C−T_x (where T_x is O, OH, or F), graphitic C−C, and C−O/C−F, respectively. The Ti−C peak obtained by the oxidation of the Ti_3C_2 was presumed to result from the formation of TiO_2 and carbon during the etching process. The small amount of TiO_2 is beneficial owing to its photocatalytic efficiency.[49] Figure 5g, showing a Ti 2P high-resolution spectrum, indicated peaks at 458.73 and 46.5 eV corresponding to Ti $2P_{3/2}$ and Ti $2P_{1/2}$,

https://doi.org/10.1021/acsanm.2c01639
ACS Appl. Nano Mater. 2022, 5, 9319−9333

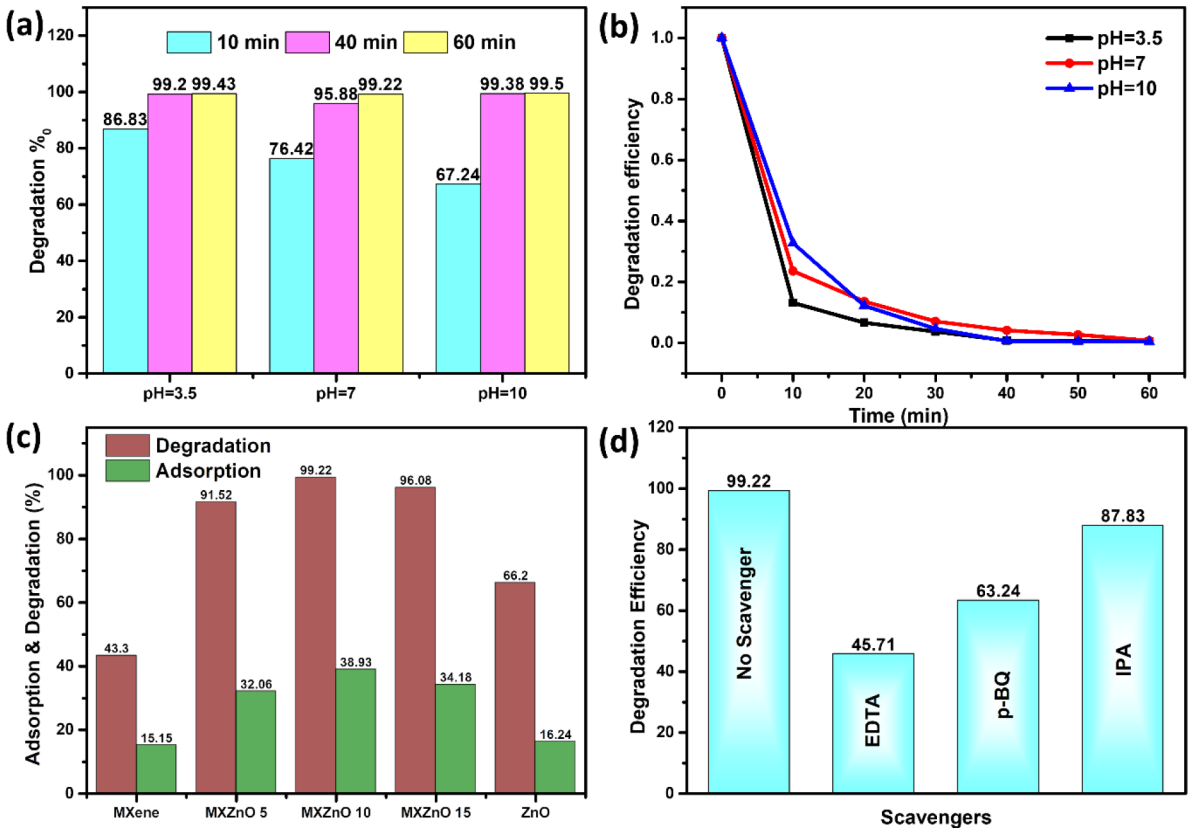

Figure 7. (a) Degradation percentage and (b) degradation efficiency of MB at different pH values. (c) Adsorption and degradation percentage study of pristine Ti_3C_2, pristine ZnO, and ZnO-Ti_3C_2 nanocomposites. (d) Degradation efficiency of the MXZnO-10 catalyst with different scavengers.

respectively, indicating the partial oxidation of Ti_3C_2. Ti 2P peaks at 455.12 and 454.38 eV are attributed to C−Ti^{3+}−T_x and C−Ti^{2+}−T_x.[50] The O 1S spectra of Ti_3C_2 exhibit that the two binding energy peaks at the 530.8 and 532.8 eV can be assigned to Ti−O, and C−Ti−$(OH)_x$, respectively, as demonstrated in Figure 5h.[51] Two prominent binding energy peaks of Zn 2p in Figure 2e spotted at 1021.77 and 1044.87 eV with a spin separation of 23.1 eV were attributed to Zn $2P_{3/2}$ and Zn $2P_{1/2}$, respectively. The significant components in the F 1S spectrum observed at a binding energy of 684.68 and 685.82 correspond to Ti−F and Al−F, respectively, as shown in Figure S5.

The photocatalytic dye degradation test of MB was performed using the pristine Ti_3C_2, pristine ZnO, and different composites of ZnO-Ti_3C_2 as shown in Figure 6a−e. The absorbance spectra of 40 mL of MB (20 μM) were recorded in the time range of 0 to 60 min in the presence of the different ZnO-Ti_3C_2 composites. Among all catalysts, MXZnO-10 showed excellent degradation performance with 76.4% in 10 min and 99.2% in 60 min for MB dye. The MXZnO-10 catalyst was used to degrade the other two dyes like MO and CR and drugs like IBP and CIF. Pristine ZnO nanoflakes were also tested for the degradation of MB, which showed 66.2% degradation efficiency in 60 min. Before starting the photocatalytic degradation, the catalyst and dye solution was stirred for 10 min in the dark to avoid the photocatalytic effect. The MB solution fades over time, eventually becoming a colorless solution. From the UV−vis absorption graphs, MB clearly showed strong absorption at 665 and 292 nm with one shoulder peak at 614 nm, which drastically reduced in 10 min after exposure to the catalyst. A graph is plotted between C/C_0 and the time interval showing the MB degradation where C is the residual MB concentration at time t and C_0 is the initial MB concentration at t = 0, shown in Figure 6f. Furthermore, the plot displays photocatalytic degradation of MB without any catalyst, and it showed the lowest degradation percentage. Figure 6f reveals that, at the same time, the pristine Ti_3C_2 has the lowest degradation performance, only 7.4% in 10 min, compared to ZnO-Ti_3C_2 nanocomposites, which are primarily controlled by surface property and its termination groups.[30] In the initial 10 min, MB without a catalyst, MXZnO-5, MXZnO-10, and MXZnO-15 showed degradation percentages of 1%, 62.3%, 76.4%, and 25.4%, respectively. The comparative study reveals an MXZnO-10s maximum degradation performance of almost 76.4% in 10 min, as shown in Figure 6i. After 60 min, MB without a catalyst, MXZnO-5, MXZnO-10, and MXZnO-15 demonstrated 43.3%, 97.3%, 99.2%, and 96.1% degradation, respectively. Table S3 shows a comparative performance of various oxides and MXene-based catalysts on the degradation of some common dyes obtained from the literature. Compared with other composite materials reported, the prepared catalyst showed the highest degradation of 93% within 30 min. Incorporation of ZnO in Ti_3C_2 enhanced photocatalytic degradation owing to the low bandgap of ZnO-Ti_3C_2 compared to pristine ZnO, which increases the faster charge transfer toward the water molecule to produce active radicals after exposure to sunlight. The previous study shows that Ti_3C_2 has an effective electron acceptor, which supports photocatalytic activity by suppressing the recombination rate with the combined effect of ZnO-Ti_3C_2.[52] The higher

https://doi.org/10.1021/acsanm.2c01639
ACS Appl. Nano Mater. 2022, 5, 9319−9333

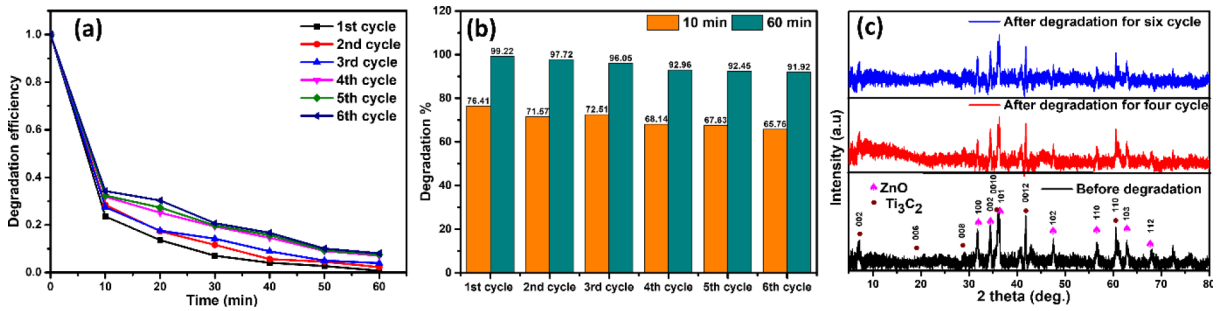

Figure 8. (a) Degradation efficiency up to the sixth cycle and (b) degradation percentage up to the sixth cycle of as-synthesized MXZnO-10 catalyst and (c) XRD measurement before and after degradation for four and six cycles.

absorption results in high charge generation and less recombination of MXZnO-10 due to the lower bandgap. MXZnO-10 generates more electron and hole pairs than others, which quickly transfer from ZnO to Ti_3C_2 to overcome the recombination rate.

Furthermore, the uncombined electron and hole pairs help to degrade the MB dye. The degradation of MB occurs through the oxidation process, leading to breaking the aromatic ring into smaller products via three steps—decolorization, degradation, and mineralization.[53] The mineralization/degradation of the organic dye was further investigated by high-performance liquid chromatography (HPLC), in which peaks disappear at a higher retention time (dye substrate) and appear at a lower retention time after 60 min of irradiation, as shown in Figure S3. Further, to determine the apparent degradation, a rate graph plotted between $\ln(C_0/C)$ and time is shown in Figure 6g. To measure the degradation rate, the kinetics of the reaction is described using a pseudo-first-order equation:

$$-\ln C/C_0 = K_{app}t$$

where C is the concentration of MB at time t and C_0 is the concentration of MB at $t = 0$. K_{app} is the apparent reaction rate constant at time t. The degradation rate constants (K) and linear regression coefficient degree (R^2) were calculated from the slope using linear regression, as shown in Table S4. It reveals that MXZnO-10 demonstrated the highest degradation rate at 0.071 min^{-1} among three MXene nanocomposites tested with MB organic dye, and pristine Ti_3C_2 shows the lowest K with 0.0094 min^{-1} (Figure 6h). The lower K value of MXZnO-15 at 0.054 min^{-1} is due to ZnO's higher stacking into Ti_3C_2, leading to more agglomeration of ZnO particles, promoting lesser interfacial interaction and a faster recombination rate between photogenerated electrons and holes. The degradation of organic MB dye is dependent upon various other factors like MB concentration, catalyst concentration, source of irradiation, illuminance time, and the nature of the catalyst. The enhancement in the performance of the MXZnO-10 catalyst is due to the efficient separation of electron and hole charge carriers with a longer lifespan. MXene as an effective electron acceptor can be easily channelized through its layer structure by hindering electron−hole recombination and thereby enhancing photocatalytic degradation.[54] More importantly, the layered stack structure formed generally increases the charge transfer efficiency. The generated active species participating in the reaction during photocatalytic degradation, such as hydroxyl radicals ($^{\bullet}OH$), photogenerated holes (h^+), and superoxide radical anions ($O_2^{\bullet-}$), play a central role in the photocatalytic degradation of MB. In MXZnO-10, the catalyst ZnO has been well distributed over the MXene layers, providing better interfacial interaction to help the MB degradation, as observed from the SEM image Figure 2c.

The pH of the solution disturbs the hydroxyl radicals and catalyst surface interaction, which affects the photodegradation of organic dyes, as demonstrated in Figure 7a,b. The pH-dependent study was investigated at three different pH's of 3.5, 7, and 10 at a concentration of 20 μM with a MXZnO-10 catalyst loading of 40 mg/L. The equilibrium between the photocatalyst and the dye solution was achieved for 10 min. The results revealed that, as the pH increased to basic pH, the overall methylene blue degradation efficiency increased and showed the highest removal efficiency. Generally, the degradation capacity is lesser at lower pH than the neutral and acidic medium because of the electrostatic repulsion force between a positively charged photocatalyst and cationic MB. The positive charge at photocatalyst ZnO-Ti_3C_2 may be due to a highly protonated hydroxyl surface group.[55] At pH 3.5, methylene blue achieved the highest degradation of 86.83% in 10 min, indicating that electrostatic interactions are less dominated than H bonding between the MXene hydroxyl group and MB, leading to higher degradation.[54] At pH= 10, negative charges such as $[Ti-F]^-$ and $[Ti-O]^-H^+$ were produced at the surface of ZnO-Ti_3C_2, further enhanced by ZnO nanoflakes when it reacted with cationic MB dye.[30] Several radical trapping investigations were done to demonstrate the photocatalytic dye process and define the most relevant effects of various species on photocatalytic activity. Several radical trapping investigations were evaluated to demonstrate the photocatalytic dye degradation process and to define the most relevant effects of various species on the photocatalytic activity, as demonstrated in Figure 7d. Initially, three varieties of scavengers were selected, triethanolamine (EDTA, an h^+ scavenger), *tert*-butanol (IPA, an $OH^{\bullet}$ scavenger), and p-benzoquinone (p-BQ, an O^{2-} scavenger), to detect the main reactive species for dye degradation experiments. Typically, 3 mL of scavenger (20 mM) is mixed in MB solutions containing the ZnO-Ti_3C_2 photocatalyst and then exposed to light for 60 min. The addition of an EDTA quencher in the solution had a major effect on the efficiency of MB degradation, indicating the importance of holes. The addition of p-BQ and IPA scavengers reduces the efficiency of MB photocatalysis to roughly 36.26% and 11.48%, respectively, showing that radicals play an important role in photocatalytic processes. As a result, it has been established that the contribution of $^{\bullet}O^{2-}$ and $^{\bullet}OH$ radicals drive the MB solution's photocatalytic mechanism toward MXZnO-10 composites, whereas h^+ showed a major effect in the degradation process. Figure 7c depicts a bar diagram of methylene blue's dark adsorption and photocatalytic degradation percentage on the

https://doi.org/10.1021/acsanm.2c01639
ACS Appl. Nano Mater. 2022, 5, 9319−9333

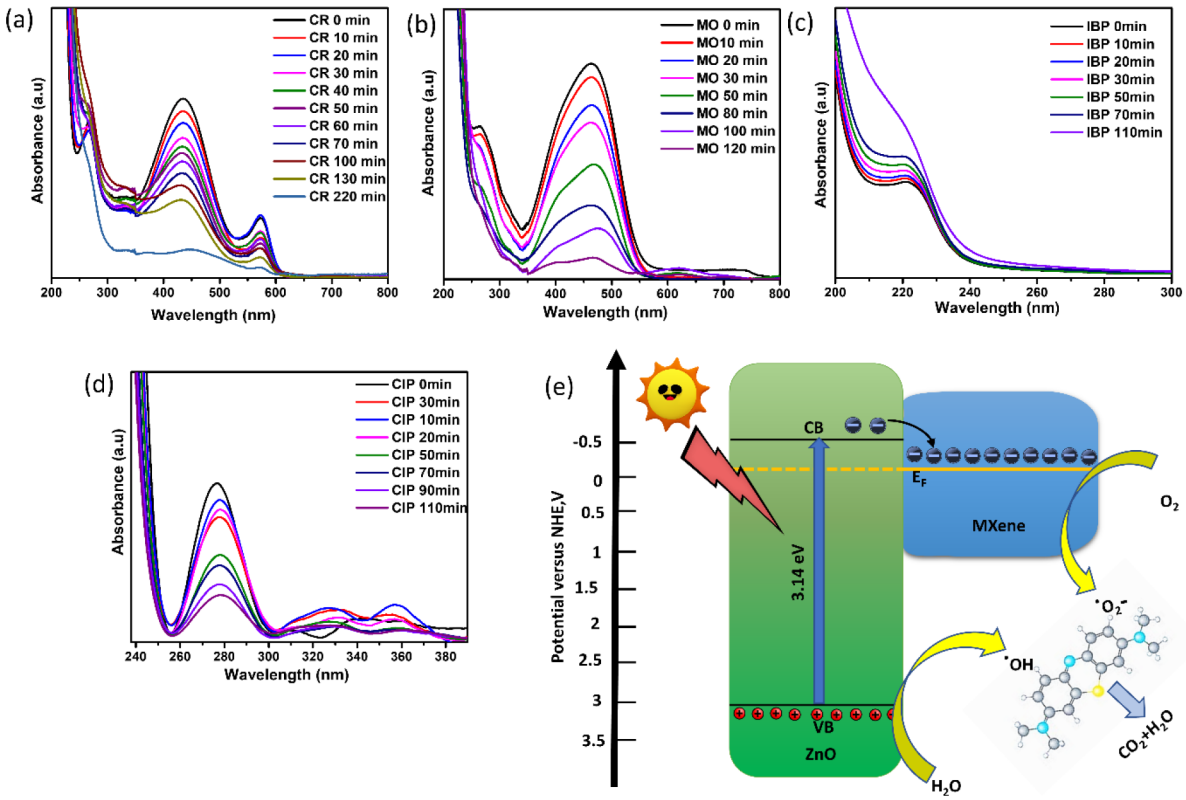

Figure 9. Adsorption curve of cresol red (a), methyl orange (b), ibuprofen (c), and ciprofloxacin (d) with the as-synthesized MXZnO-10 catalyst. (e) Charge carrier transfer mechanism from ZnO to MXene in the ZnO-Ti_3C_2 nanocomposite

MXZnO-10 catalyst. Adsorption−desorption equilibrium was observed for 60 min and obtained less degradation efficiency than photodegradation. The degradations of ZnO, Ti_3C_2, MXZnO-5, MXZnO-10, and MXZnO-15 were obtained to be 16.24%, 15.15%, 32.06%, 38.93%, and 34.18%, respectively.

The stability of the MXZnO-10 catalyst was investigated through the degradation of MB over six cycles under optimum conditions. A photocatalytic degradation efficiency and bar diagram of reusability of the MXZnO-10 catalyst are shown in Figure 8a and b. After the photodegradation reaction, the MXZnO-10 composite was collected by centrifugation after each cycle and washed twice using DI water, followed by ethanol to remove any sticky degradation products. Finally, the catalyst was dried overnight at room temperature before use in the next cycle. Degradation efficiency was 93% in the fourth cycle and 92% in the sixth cycle. In the third cycle, the degradation efficiency increased from 71.57 to 72.51 (in the initial 10 min), indicating strong interfacial interaction even after the second cycle. However, the overall efficiency is reduced in the third cycle from 97.72 to 96.05% (in 60 min). When the MXZnO-10 catalyst was utilized up to the sixth cycle, the degrading efficiency dropped by nearly 7.3%, as shown in Figure 8b. This might be due to an irreversible change in the catalyst during each cycle, which affects the activity of the catalyst. Furthermore, XRD measurements were carried out for the fourth and sixth cycles to observe the deterioration of the catalyst, which indicates a very minute change in XRD peak intensity, as shown in Figure 8c. SEM and EDX of catalyst MXZnO-10 are also provided in Figure S6, showing a very slight ZnO particle loss. It can be concluded that the MXZnO-10 catalyst appears to be stable, allowing it to be reused for multiple cycles.

Figure 9a,b show the degradation of dyes (cresol red, CR; methyl orange, MO), and Figure 9c,d show degradation of anti-inflammatory and antibiotic drug degradation (ibuprofen, IBP; ciprofloxacin, CIF) using the MXZnO-10 catalyst. CR obtained two characteristic absorption peaks at 434 and 573 nm, as shown in Figure 9a.[56] The absorption peaks' intensity with times indicates the degradation of CR by the MXZnO-10 catalyst. The complete degradation was obtained at 220 min with a red shift, indicating the degradation into lower hydrocarbon molecules. The methyl orange absorbance measurement exhibits the two peaks at ∼265 and ∼266 nm shown in Figure 9b.[57] The decrease of 265 nm peaks indicates the cleavage of the azo bond, and methyl orange solution becomes decolorized after irradiating sunlight for 120 min. Figure 9c shows the absorption spectra of IBP with different time irradiation under solar light. One absorption band was observed at 222 nm associated with the $\pi-\pi^*$ transition owing to the aromatic character of IBU.[58] The degradation graph of CIP shown in Figure 9d indicates the characteristic peak at ∼276 nm.[59] Additionally, 72% degradation was obtained in 110 min using the MXZnO-10 catalyst. The different electrostatic interactions between the Ti_3C_2 surface and organic pollutant molecule account for the significant difference in effective removal.

Figure 9e schematically depicts a proposed mechanism for the ZnO-Ti_3C_2 nanocomposite structure's improved photocatalytic performance in the presence of electrons and holes. The improved photocatalytic performance may be ascribed as follows: The Fermi level of Ti_3C_2 MXene is lower than the conduction band (CB) of ZnO, and ZnO's work function is more significant than Ti_3C_2.[60,61] When light interacts with the ZnO-Ti_3C_2 hybrid structure, generated electrons flow rapidly

https://doi.org/10.1021/acsanm.2c01639
ACS Appl. Nano Mater. 2022, 5, 9319−9333

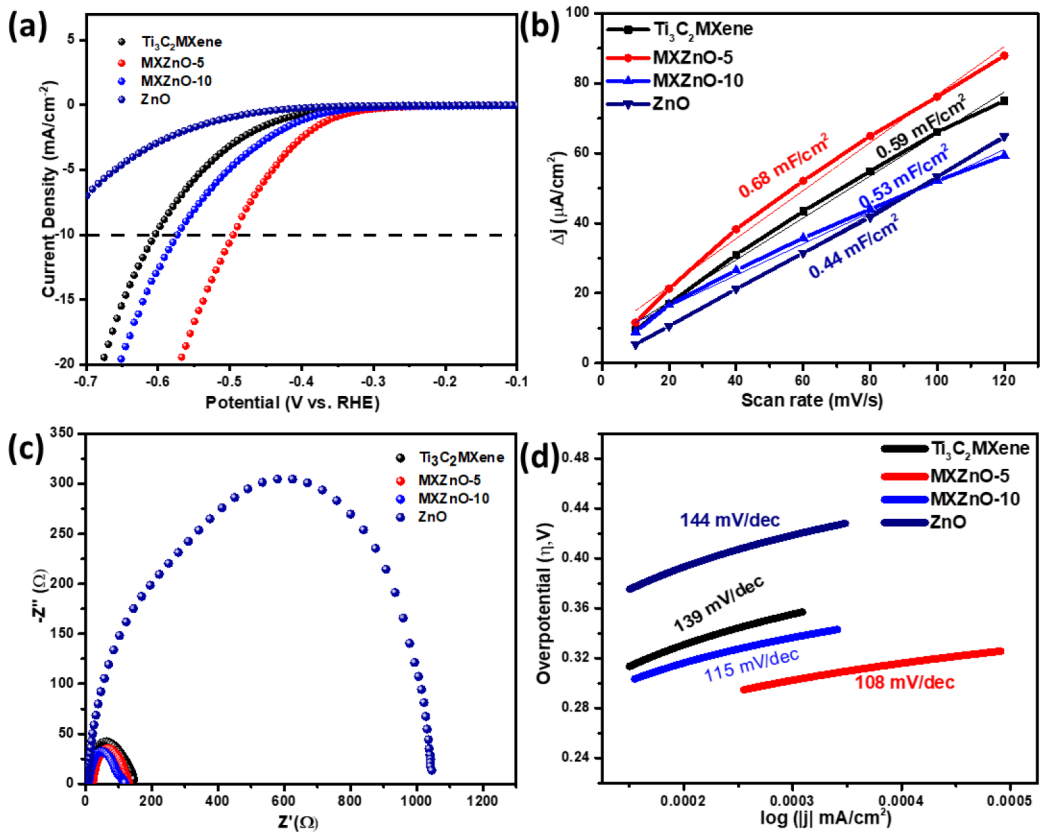

Figure 10. (a) HER polarization curves of as synthesized samples at a scan rate of 10 mV/s. (b) Corresponding scan rate vs current density with C_{dl} values. (c) Impedance spectra of catalyst. (d) Tafel plot for the catalyst derived from the polarization plot.

from ZnO's CB to Ti_3C_2, and the Schottky barrier prevents them from returning. Superoxide anion radicals ($^{\bullet}O_2^-$) are expected to form due to these produced electrons attacking O_2 molecules. Meanwhile, holes in ZnO's valence band (VB) interact with H_2O or OH ions, resulting in $^{\bullet}OH$ radicals. MB can then be degraded to harmless compounds by reacting with active radicals such as $^{\bullet}OH$ and $^{\bullet}O_2^-$.[62] The entire photodegradation procedure can be summarized as follows:

$$ZnO + h\nu \rightarrow ZnO\ (e^- + h^+)$$

$$Ti_3C_2 + e^- \rightarrow Ti_3C_2(e^-)\ (e^-\ \text{trapped by MXene})$$

$$Ti_3C_2\ (e^-) + O_2 \rightarrow {}^{\bullet}O_2^- + Ti_3C_2$$

$$ZnO\ (h^+) + H_2O \rightarrow {}^{\bullet}OH^-$$

$$^{\bullet}OH^- + MB \rightarrow CO_2 + H_2O$$

$$^{\bullet}O_2^- + MB \rightarrow CO_2 + H_2O$$

In general, metal oxides are used in photocatalytic water splitting compared to the electrocatalytic application due to the low electric conductivity. Many researchers have used transition metal oxides for the HER application.[63,64] The ZnO-MXene nanocomposites synthesized and studied are the first of their kind for HER application to obtain cheaper electrocatalysts for green hydrogen production. Figure 10a shows the anodic polarization curves for HER of the materials. The MXZnO-5 exhibited an onset overpotential of 422 mV and MXZnO-10 of 588 mV. For determining the HER activity of the electrocatalyst, the overpotential at 10 mA/cm^2 is a significant factor. MXZnO-5 and MXZnO-10 exhibited an overpotential of 495 mV and 573 mV, respectively, at an anodic 10 mA/cm^2 current density. Even though the observed overpotentials are far higher than the standard Pt/C (~38 mV @-10 mA/cm^2),[65] a significant ~40% reduction in the onset overpotential is observed by MXZnO-5 and an ~18% reduction for MXZnO-10 at 10 mA/cm^2 with the introduction of ZnO into the MXene layers. Hence, this reduction in overpotential can be attributed to the synergy between ZnO and Ti_3C_2 due to an increase in OH functional groups on the surface of ZnO-Ti_3C_2. Figure 10b shows the catalytic materials' capacitive current vs scan rate. MXZnO-5, MXZnO-10, and pristine Ti_3C_2 show a double layer capacitance (C_{dl}) of 0.68 mF/cm^2, 0.53 mF/cm^2, and 0.59 mF/cm^2, respectively. The significantly lower C_{dl} of the MXZnO-10 nanocomposite can be explained by the ZnO nanoparticles hindering the catalytically active sites in the nonfaradaic region (Figure S7). Electrochemically active surface area (ECSA) was measured to evaluate the electrochemical double-layer capacitance of the catalyst. The electrochemical capacitance was calculated using the cyclic voltammograms to measure the non-Faradaic capacitive current associated with double-layer charging. The scan rate is directly proportional to the double layer charging current, normalized on the geometric area of the electrode. Hence, the ECSA of the catalyst can be calculated as

$$ECSA = C_{dl}/C_s$$

C_{dl} was derived from a linear fitted slope by plotting the current as a function of scan rate. The specific capacitances (C_s) were chosen according to the previously reported value (0.035 mF cm^{-2} in 0.5 M H_2SO_4).[66] The obtained C_{dl} values of MXZnO-5, MXZnO-10, Ti_3C_2, and ZnO are 0.34, 0.265,

https://doi.org/10.1021/acsanm.2c01639
ACS Appl. Nano Mater. 2022, 5, 9319−9333

0.295, and 0.22 mF/cm^2. ECSA values are determined as 9.71, 7.57, 8.42, and 6.28 mF/cm^2.

In contrast, the synergy between ZnO and MXene can be observed in the faradaic region reflected in the polarization curves. Nafion binder concentration and the deposition rate of the materials were kept standard throughout the study to understand the relative catalytic performances because it has a crucial effect on HER performance. Figure 10c shows the Nyquist plots of the composites at 531 mV with respect to E_{RHE}. The diffusive layer resistance at the electrode/electrolyte interface is undeterminable due to the absence of the Warburg response in the lower frequency region, attributed to the H_2 gas bubbles screening the conducting electrode surface in the Faradaic potential domain. The Z_{real} intercept at high frequency for all three materials indicates a significant electrode resistance R_e.[67] The charge transfer resistance R_{CT} of the systems, which is the characteristic of the HER process, was determined from the semicircular loop at the midfrequency region. The R_{CT}'s of pristine Ti_3C_2, MXZnO-5, and MXZnO-10 are 127Ω, 109 Ω, and 110 Ω, respectively, with MXZnO-5 having the least resistance among all. The charge transfer resistance (R_{ct}) exhibited supports the observed overpotentials of the corresponding composites. The equivalent circuit fittings are represented in Figure S10. Figure 10d shows the Tafel slopes of the materials. Tafel plots were fitted to the Tafel equation ($\eta = b \log j + a$) to explore the HER mechanism, where b is the Tafel slope and j designates the ratio of current density to the exchange current density. The Tafel slope of pristine Ti_3C_2 is 139 mV/dec, which is higher than MXZnO-5 (108 mV/dec) and MXZnO-10 (115 mV/dec) and lower than pristine ZnO (144 mV/dec). The cyclic stability of the MXZnO-5 was studied by performing (Figure S8) a CV test over the nonfaradaic region. After 1000 cycles, high electrocatalytic performance is observed with a reduction in overpotential. This is attributed to the continuous exfoliation of the MXene layers in the presence of Pt (counter electrode) at a pH of 0.[68] Additionally, a temporal study on the performance of MXZnO-5 was carried out using chronopotentiometry at a 5 mA cm^{-1} current density. The stability of MXZnO-5 was studied, and Figure S9 shows its 10 h stability.

CONCLUSION

In summary, 2D ZnO-Ti_3C_2 nanohybrid catalysts with varying wt % of ZnO were synthesized through in situ hydrothermal methods and demonstrated their performance as photocatalysts and electrocatalysts for the hydrogen evolution reaction. The physicochemical properties of the samples were thoroughly analyzed by various characterization techniques such as SEM, TEM, TGA, XRD, and XPS, ascertaining the successful formation of the ZnO-Ti_3C_2 nanohybrid. A series of experiments were carried out with various ZnO-Ti_3C_2 composites to investigate photocatalytic degradation and its kinetics. The experimental data revealed that the MXZnO-10 nanohybrid sample has a high MB degradation capacity of 99.2% after an irradiation time of 60 min with a high level of reproducibility, reusability, and stability through six catalytic cycles. The chronopotentiometry, polarization curves, Nyquist, and Tafel plots demonstrated that ZnO-Ti_3C_2 nanocomposites were stable and durable HER electrocatalysts compared to pristine MXene. Among the materials, MXZnO-5 shows the lowest overpotential of 495 mV at an anodic 10 mA/cm^2 current density, a small Tafel slope of 108 mV/dec, and contact resistance of 109 Ω. The photo- and electrocatalysis performance of hydrothermally synthesized 2D ZnO-Ti_3C_2 nanohybrids has been confirmed as an excellent nanostructure composition for photocatalytic and electrocatalytic applications.

ASSOCIATED CONTENT

Supporting Information

The Supporting Information is available free of charge at https://pubs.acs.org/doi/10.1021/acsanm.2c01639.

Figures S1 to S10 include SEM, EDX elemental table and EDX elemental mapping, TEM and SAED patterns, HPLC spectrum, N_2 adsorption isotherm and pore size distribution, XPS, SEM and EDX after reusability, cyclic voltammograms, HER polarization curves, chronopotentiometry, and an EIS fitting plot. Tables S1 to S4 include crystallite size, dislocation density and strain calculation, BET surface area and BJH pore size distribution data, a comparison with other photocatalysts, evaluation of rate constant, and R^2 and photodegradation efficiency (PDF)

AUTHOR INFORMATION

Corresponding Author

Rakesh K. Sharma − *Sustainable Materials and Catalysis Research Laboratory (SMCRL), Department of Chemistry, Indian Institute of Technology Jodhpur, Jodhpur 342037, India;* orcid.org/0000-0002-0984-8281; Email: rks@iitj.ac.in

Authors

Bhagirath Saini − *Sustainable Materials and Catalysis Research Laboratory (SMCRL), Department of Chemistry, Indian Institute of Technology Jodhpur, Jodhpur 342037, India*

Harikrishna K − *Sustainable Materials and Catalysis Research Laboratory (SMCRL), Department of Chemistry, Indian Institute of Technology Jodhpur, Jodhpur 342037, India*

Devika Laishram − *Sustainable Materials and Catalysis Research Laboratory (SMCRL), Department of Chemistry, Indian Institute of Technology Jodhpur, Jodhpur 342037, India; University College Dublin, School of Chemical and Bioprocess Engineering, Dublin 4, Ireland;* orcid.org/0000-0001-6953-8309

R Krishnapriya − *Sustainable Materials and Catalysis Research Laboratory (SMCRL), Department of Chemistry, Indian Institute of Technology Jodhpur, Jodhpur 342037, India; Mechanical and Aerospace Engineering Department, College of Engineering, United Arab Emirate University, Al Ain 15551, United Arab Emirates*

Rahul Singhal − *Department of Physics and Engineering Physics, Central Connecticut State University, New Britain, Connecticut 06050, United States;* orcid.org/0000-0002-5017-9091

Complete contact information is available at: https://pubs.acs.org/10.1021/acsanm.2c01639

Author Contributions

B.S. performed the experimental works, analyzed data, and drafted the main manuscript. K.H. assisted B.S. in the experimental work, interpretation of results, and manuscript writing. D.L., R.K., R.K.S., and R.S. were involved in the conceptualization of research ideas, data interpretation,

https://doi.org/10.1021/acsanm.2c01639
ACS Appl. Nano Mater. 2022, 5, 9319−9333

manuscript review, and editing. R.K.S. was involved in funding acquisition and supervised the entire work. All authors reviewed the manuscript.

Funding

SERB-CRG-India (grant number CRG/2020/002163) and DBT PAN IIT Center for Bioenergy (grant number BT/PR41982/PBD/26/822/2021)

Notes

The authors declare no competing financial interest.

■ ACKNOWLEDGMENTS

The authors would like to thank the Ministry of Education for financial support. We also thank the Centre for Advanced Scientific Equipment (CASE)-IITJ and Scientium Analyze Solutions for characterizations. The authors are grateful for financial support from SERB-CRG-India (grant number CRG/2020/002163) and DBT PAN IIT Center for Bioenergy (grant number BT/PR41982/PBD/26/822/2021).

■ DEDICATION

Dedicated to Professor Yury Gogotsi, Drexel University, on his 60th birthday

■ REFERENCES

(1) *Global Energy Review: CO_2 Emissions in 2020*; IEA, 2020.
(2) Yamada, Y.; Tadokoro, H.; Fukuzumi, S. An effective preparation method of composite photocatalysts for hydrogen evolution using an organic photosensitizer and metal particles assembled on alumina-silica. *Catal. Today* **2016**, *278*, 303−311.
(3) Yang, X.; Banerjee, A.; Ahuja, R. Structural Insight of the Frailty of 2D Janus NbSeTe as an Active Photocatalyst. *ChemCatChem.* **2020**, *12* (23), 6013−6023.
(4) Wang, L.; Si, W.; Tong, Y.; Hou, F.; Pergolesi, D.; Hou, J.; Lippert, T.; Dou, S. X.; Liang, J. Graphitic carbon nitride (g-C3N4)-based nanosized heteroarrays: Promising materials for photoelectrochemical water splitting. *Carbon Energy* **2020**, *2* (2), 223−250.
(5) Naguib, M.; Kurtoglu, M.; Presser, V.; Lu, J.; Niu, J.; Heon, M.; Hultman, L.; Gogotsi, Y.; Barsoum, M. W. Two-Dimensional Nanocrystals Produced by Exfoliation of Ti3AlC2. *Adv. Mater.* **2011**, *23* (37), 4248−4253.
(6) Naguib, M.; Mashtalir, O.; Carle, J.; Presser, V.; Lu, J.; Hultman, L.; Gogotsi, Y.; Barsoum, M. W. Two-Dimensional Transition Metal Carbides. *ACS Nano* **2012**, *6* (2), 1322−1331.
(7) Zhang, J.; Kong, N.; Uzun, S.; Levitt, A.; Seyedin, S.; Lynch, P. A.; Qin, S.; Han, M.; Yang, W.; Liu, J.; Wang, X.; Gogotsi, Y.; Razal, J. M. Scalable Manufacturing of Free-Standing, Strong Ti3C2Tx MXene Films with Outstanding Conductivity. *Adv. Mater.* **2020**, *32* (23), 2001093.
(8) Ghidiu, M.; Lukatskaya, M. R.; Zhao, M.-Q.; Gogotsi, Y.; Barsoum, M. W. Conductive two-dimensional titanium carbide 'clay' with high volumetric capacitance. *Nature* **2014**, *516* (7529), 78−81.
(9) Shen, S.; Ke, T.; Rajavel, K.; Yang, K.; Lin, D. Dispersibility and Photochemical Stability of Delaminated MXene Flakes in Water. *Small* **2020**, *16* (36), 2002433.
(10) Zhou, Z.; Song, Q.; Huang, B.; Feng, S.; Lu, C. Facile Fabrication of Densely Packed Ti3C2MXene/Nanocellulose Composite Films for Enhancing Electromagnetic Interference Shielding and Electro-/Photothermal Performance. *ACS Nano* **2021**, *15* (7), 12405−12417.
(11) Chao, M.; He, L.; Gong, M.; Li, N.; Li, X.; Peng, L.; Shi, F.; Zhang, L.; Wan, P. Breathable Ti3C2Tx MXene/Protein Nanocomposites for Ultrasensitive Medical Pressure Sensor with Degradability in Solvents. *ACS Nano* **2021**, *15* (6), 9746−9758.
(12) Hieu, V. Q.; Lam, T. C.; Khan, A.; Thi Vo, T.-T.; Nguyen, T.-Q.; Doan, V. D.; Tran, D. L.; Le, V. T.; Tran, V. A. TiO2/Ti3C2/g-C3N4 ternary heterojunction for photocatalytic hydrogen evolution. *Chemosphere* **2021**, *285*, 131429.
(13) Naguib, M.; Come, J.; Dyatkin, B.; Presser, V.; Taberna, P.-L.; Simon, P.; Barsoum, M. W.; Gogotsi, Y. MXene: a promising transition metal carbide anode for lithium-ion batteries. *Electrochem. Commun.* **2012**, *16* (1), 61−64.
(14) Zhu, J.; Ha, E.; Zhao, G.; Zhou, Y.; Huang, D.; Yue, G.; Hu, L.; Sun, N.; Wang, Y.; Lee, L. Y. S.; Xu, C.; Wong, K.-Y.; Astruc, D.; Zhao, P. Recent advance in MXenes: A promising 2D material for catalysis, sensor and chemical adsorption. *Coord. Chem. Rev.* **2017**, *352*, 306−327.
(15) Levitt, A. S.; Alhabeb, M.; Hatter, C. B.; Sarycheva, A.; Dion, G.; Gogotsi, Y. Electrospun MXene/carbon nanofibers as supercapacitor electrodes. *Journal of Materials Chemistry A* **2019**, *7* (1), 269−277.
(16) Gao, X.; Du, X.; Mathis, T. S.; Zhang, M.; Wang, X.; Shui, J.; Gogotsi, Y.; Xu, M. Maximizing ion accessibility in MXene-knotted carbon nanotube composite electrodes for high-rate electrochemical energy storage. *Nat. Commun.* **2020**, *11* (1), 6160.
(17) Wang, J.; Zhao, T.; Yang, Z.; Chen, Y.; Liu, Y.; Wang, J.; Zhai, P.; Wu, W. MXene-Based Co, N-Codoped Porous Carbon Nanosheets Regulating Polysulfides for High-Performance Lithium−Sulfur Batteries. *ACS Appl. Mater. Interfaces* **2019**, *11* (42), 38654−38662.
(18) Luo, S.; Wang, R.; Yin, J.; Jiao, T.; Chen, K.; Zou, G.; Zhang, L.; Zhou, J.; Zhang, L.; Peng, Q. Preparation and Dye Degradation Performances of Self-Assembled MXene-Co3O4 Nanocomposites Synthesized via Solvothermal Approach. *ACS Omega* **2019**, *4* (2), 3946−3953.
(19) Wu, Z.; Liang, Y.; Yuan, X.; Zou, D.; Fang, J.; Jiang, L.; Zhang, J.; Yang, H.; Xiao, Z. MXene Ti3C2 derived Z−scheme photocatalyst of graphene layers anchored TiO2/g−C3N4 for visible light photocatalytic degradation of refractory organic pollutants. *Chemical Engineering Journal* **2020**, *394*, 124921.
(20) Zhang, H.; Li, M.; Cao, J.; Tang, Q.; Kang, P.; Zhu, C.; Ma, M. 2D a-Fe2O3 doped Ti3C2MXene composite with enhanced visible light photocatalytic activity for degradation of Rhodamine B. *Ceram. Int.* **2018**, *44* (16), 19958−19962.
(21) Tan, D.; Lee, W.; Kim, Y. E.; Ko, Y. N.; Youn, M. H.; Jeon, Y. E.; Hong, J.; Jeong, S. K.; Park, K. T. SnO2/ZnO Composite Hollow Nanofiber Electrocatalyst for Efficient CO2 Reduction to Formate. *ACS Sustainable Chem. Eng.* **2020**, *8* (29), 10639−10645.
(22) Rakhi, R. B.; Ahmed, B.; Anjum, D.; Alshareef, H. N. Direct Chemical Synthesis of MnO2 Nanowhiskers on Transition-Metal Carbide Surfaces for Supercapacitor Applications. *ACS Appl. Mater. Interfaces* **2016**, *8* (29), 18806−18814.
(23) Ahmed, B.; Anjum, D. H.; Gogotsi, Y.; Alshareef, H. N. Atomic layer deposition of SnO2 on MXene for Li-ion battery anodes. *Nano Energy* **2017**, *34*, 249−256.
(24) Kadam, A. N.; Bhopate, D. P.; Kondalkar, V. V.; Majhi, S. M.; Bathula, C. D.; Tran, A.-V.; Lee, S.-W. Facile synthesis of Ag-ZnO core−shell nanostructures with enhanced photocatalytic activity. *Journal of Industrial and Engineering Chemistry* **2018**, *61*, 78−86.
(25) Krishnapriya, R.; Praneetha, S.; Murugan, A. V. Investigation of the effect of reaction parameters on the microwave-assisted hydrothermal synthesis of hierarchical jasmine-flower-like ZnO nanostructures for dye-sensitized solar cells. *New J. Chem.* **2016**, *40* (6), 5080−5089.
(26) Kulkarni, D. R.; Malode, S. J.; Keerthi Prabhu, K.; Ayachit, N. H.; Kulkarni, R. M.; Shetti, N. P. Development of a novel nanosensor using Ca-doped ZnO for antihistamine drug. *Mater. Chem. Phys.* **2020**, *246*, 122791.
(27) Qian, Y.; Wei, H.; Dong, J.; Du, Y.; Fang, X.; Zheng, W.; Sun, Y.; Jiang, Z. Fabrication of urchin-like ZnO-MXene nanocomposites for high-performance electromagnetic absorption. *Ceram. Int.* **2017**, *43* (14), 10757−10762.
(28) Liu, X.; Chen, C. Mxene enhanced the photocatalytic activity of ZnO nanorods under visible light. *Mater. Lett.* **2020**, *261*, 127127.
(29) Khadidja, M. F.; Fan, J.; Li, S.; Li, S.; Cui, K.; Wu, J.; Zeng, W.; Wei, H.; Jin, H.-G.; Naik, N.; Chao, Z.; Pan, D.; Guo, Z. Hierarchical

https://doi.org/10.1021/acsanm.2c01639
ACS Appl. Nano Mater. 2022, 5, 9319−9333

ZnO/MXene composites and their photocatalytic performances. *Colloids Surf., A* **2021**, *628*, 127230.
(30) My Tran, N.; Thanh Hoai Ta, Q.; Sreedhar, A.; Noh, J.-S. Ti3C2Tx MXene playing as a strong methylene blue adsorbent in wastewater. *Appl. Surf. Sci.* **2021**, *537*, 148006.
(31) Luo, Q.; Yang, J.; Wu, Y.; Cai, Q. Hybridisation of ZnO with Ti3C2 as a co-catalyst for enhanced photocatalytic activity. *Micro & Nano Letters* **2020**, *15* (11), 764−768.
(32) Husmann, S.; Budak, Ö.; Shim, H.; Liang, K.; Aslan, M.; Kruth, A.; Quade, A.; Naguib, M.; Presser, V. Ionic liquid-based synthesis of MXene. *Chem. Commun.* **2020**, *56* (75), 11082−11085.
(33) Melchior, S. A.; Raju, K.; Ike, I. S.; Erasmus, R. M.; Kabongo, G.; Sigalas, I.; Iyuke, S. E.; Ozoemena, K. I. High-Voltage Symmetric Supercapacitor Based on 2D Titanium Carbide (MXene, Ti2CTx)/Carbon Nanosphere Composites in a Neutral Aqueous Electrolyte. *J. Electrochem. Soc.* **2018**, *165* (3), A501−A511.
(34) Hieu, V. Q.; Phung, T. K.; Nguyen, T.-Q.; Khan, A.; Doan, V. D.; Tran, V. A.; Le, V. T. Photocatalytic degradation of methyl orange dye by Ti3C2−TiO2 heterojunction under solar light. *Chemosphere* **2021**, *276*, 130154.
(35) Makuła, P.; Pacia, M.; Macyk, W. How To Correctly Determine the Band Gap Energy of Modified Semiconductor Photocatalysts Based on UV−Vis Spectra. *J. Phys. Chem. Lett.* **2018**, *9* (23), 6814−6817.
(36) Dong, Y.; Mallineni, S. S. K.; Maleski, K.; Behlow, H.; Mochalin, V. N.; Rao, A. M.; Gogotsi, Y.; Podila, R. Metallic MXenes: A new family of materials for flexible triboelectric nanogenerators. *Nano Energy* **2018**, *44*, 103−110.
(37) Luo, Q.; Chai, B.; Xu, M.; Cai, Q. Preparation and photocatalytic activity of TiO_2-loaded Ti_3C_2 with small interlayer spacing. *Appl. Phys. A: Mater. Sci. Process.* **2018**, *124* (7), 495.
(38) Ta, Q. T.; Tran, N. M.; Noh, J.-S. Rice Crust-Like ZnO/Ti3C2Tx MXene Hybrid Structures for Improved Photocatalytic Activity. *Catalysts* **2020**, *10* (10), 1140.
(39) Pan, Z.; Cao, F.; Hu, X.; Ji, X. A facile method for synthesizing CuS decorated Ti3C2MXene with enhanced performance for asymmetric supercapacitors. *Journal of Materials Chemistry A* **2019**, *7* (15), 8984−8992.
(40) Cao, M.; Wang, F.; Wang, L.; Wu, W.; Lv, W.; Zhu, J. Room Temperature Oxidation of Ti3C2MXene for Supercapacitor Electrodes. *J. Electrochem. Soc.* **2017**, *164* (14), A3933−A3942.
(41) Cai, K. J.; Zheng, Y.; Shen, P.; Chen, S. Y. TiCx−Ti2C nanocrystals and epitaxial graphene-based lamellae by pulsed laser ablation of bulk TiC in vacuum. *CrystEngComm* **2014**, *16* (24), 5466−5474.
(42) Yuan, W.; Cheng, L.; Zhang, Y.; Wu, H.; Lv, S.; Chai, L.; Guo, X.; Zheng, L. 2D-Layered Carbon/TiO2 Hybrids Derived from Ti3C2MXenes for Photocatalytic Hydrogen Evolution under Visible Light Irradiation. *Advanced Materials Interfaces* **2017**, *4* (20), 1700577.
(43) Molaei, M.; Farahmandzadeh, F.; Mousavi, T. S.; Karimipour, M. Photochemical synthesis, investigation of optical properties and photocatalytic activity of CdTe/CdSe core/shell quantum dots. *Materials Technology* **2021**, 1−7.
(44) Liao, Y.; Qian, J.; Xie, G.; Han, Q.; Dang, W.; Wang, Y.; Lv, L.; Zhao, S.; Luo, L.; Zhang, W.; Jiang, H.-Y.; Tang, J. 2D-layered Ti3C2MXenes for promoted synthesis of NH3 on P25 photocatalysts. *Applied Catalysis B: Environmental* **2020**, *273*, 119054.
(45) Zhang, Y.; Di, J.; Ding, P.; Zhao, J.; Gu, K.; Chen, X.; Yan, C.; Yin, S.; Xia, J.; Li, H. Ultrathin g-C3N4 with enriched surface carbon vacancies enables highly efficient photocatalytic nitrogen fixation. *J. Colloid Interface Sci.* **2019**, *553*, 530−539.
(46) Fang, Y.; Liu, Z.; Han, J.; Jin, Z.; Han, Y.; Wang, F.; Niu, Y.; Wu, Y.; Xu, Y. High-Performance Electrocatalytic Conversion of N2 to NH3 Using Oxygen-Vacancy-Rich TiO2 In Situ Grown on Ti3C2Tx MXene. *Adv. Energy Mater.* **2019**, *9* (16), 1803406.
(47) Qian, J.; Zhao, S.; Dang, W.; Liao, Y.; Zhang, W.; Wang, H.; Lv, L.; Luo, L.; Jiang, H.-Y.; Tang, J. Photocatalytic Nitrogen Reduction by Ti3C2MXene Derived Oxygen Vacancy-Rich C/TiO2. *Advanced Sustainable Systems* **2021**, *5* (4), 2000282.
(48) Cao, Y.; Deng, Q.; Liu, Z.; Shen, D.; Wang, T.; Huang, Q.; Du, S.; Jiang, N.; Lin, C.-T.; Yu, J. Enhanced thermal properties of poly(vinylidene fluoride) composites with ultrathin nanosheets of MXene. *RSC Adv.* **2017**, *7* (33), 20494−20501.
(49) Tan, L.-L.; Chai, S.-P.; Mohamed, A. R. Synthesis and Applications of Graphene-Based TiO2 Photocatalysts. *ChemSusChem* **2012**, *5* (10), 1868−1882.
(50) Pandey, R. P.; Rasool, K.; Madhavan, V. E.; Aïssa, B.; Gogotsi, Y.; Mahmoud, K. A. Ultrahigh-flux and fouling-resistant membranes based on layered silver/MXene (Ti3C2Tx) nanosheets. *Journal of Materials Chemistry A* **2018**, *6* (8), 3522−3533.
(51) Rakhi, R. B.; Ahmed, B.; Hedhili, M. N.; Anjum, D. H.; Alshareef, H. N. Effect of Postetch Annealing Gas Composition on the Structural and Electrochemical Properties of Ti2CTx MXene Electrodes for Supercapacitor Applications. *Chem. Mater.* **2015**, *27* (15), 5314−5323.
(52) Kuang, P.; Low, J.; Cheng, B.; Yu, J.; Fan, J. MXene-based photocatalysts. *Journal of Materials Science & Technology* **2020**, *56*, 18−44.
(53) Laishram, D.; Shejale, K. P.; Gupta, R.; Sharma, R. K. Heterostructured HfO2/TiO2 spherical nanoparticles for visible photocatalytic water remediation. *Mater. Lett.* **2018**, *231*, 225−228.
(54) Liu, Q.; Tan, X.; Wang, S.; Ma, F.; Znad, H.; Shen, Z.; Liu, L.; Liu, S. MXene as a non-metal charge mediator in 2D layered CdS@Ti_3C_2@TiO_2 composites with superior Z-scheme visible light-driven photocatalytic activity. *Environmental Science: Nano* **2019**, *6* (10), 3158−3169.
(55) Ying, Y.; Liu, Y.; Wang, X.; Mao, Y.; Cao, W.; Hu, P.; Peng, X. Two-Dimensional Titanium Carbide for Efficiently Reductive Removal of Highly Toxic Chromium(VI) from Water. *ACS Appl. Mater. Interfaces* **2015**, *7* (3), 1795−1803.
(56) Wang, J.; Wang, G.; Cheng, B.; Yu, J.; Fan, J. Sulfur-doped g-C3N4/TiO2 S-scheme heterojunction photocatalyst for Congo Red photodegradation. *Chinese Journal of Catalysis* **2021**, *42* (1), 56−68.
(57) Tsuji, M.; Matsuda, K.; Tanaka, M.; Kuboyama, S.; Uto, K.; Wada, N.; Kawazumi, H.; Tsuji, T.; Ago, H.; Hayashi, J.-i. Enhanced Photocatalytic Degradation of Methyl Orange by Au/TiO2 Nanoparticles under Neutral and Acidic Solutions. *ChemistrySelect* **2018**, *3* (5), 1432−1438.
(58) Choina, J.; Kosslick, H.; Fischer, C.; Flechsig, G. U.; Frunza, L.; Schulz, A. Photocatalytic decomposition of pharmaceutical ibuprofen pollutions in water over titania catalyst. *Applied Catalysis B: Environmental* **2013**, *129*, 589−598.
(59) Yang, Z.; Yan, J.; Lian, J.; Xu, H.; She, X.; Li, H. g-C3N4/TiO2 Nanocomposites for Degradation of Ciprofloxacin under Visible Light Irradiation. *ChemistrySelect* **2016**, *1* (18), 5679−5685.
(60) Low, J.; Zhang, L.; Tong, T.; Shen, B.; Yu, J. TiO2/MXene Ti3C2 composite with excellent photocatalytic CO2 reduction activity. *J. Catal.* **2018**, *361*, 255−266.
(61) Subramanian, V.; Wolf, E. E.; Kamat, P. V. Green Emission to Probe Photoinduced Charging Events in ZnO−Au Nanoparticles. Charge Distribution and Fermi-Level Equilibration. *J. Phys. Chem. B* **2003**, *107* (30), 7479−7485.
(62) Miao, Z.; Wang, G.; Zhang, X.; Dong, X. Oxygen vacancies modified TiO2/Ti3C2 derived from MXenes for enhanced photocatalytic degradation of organic pollutants: The crucial role of oxygen vacancy to schottky junction. *Appl. Surf. Sci.* **2020**, *528*, 146929.
(63) Fernando, N.; Swaminathan, J.; Robles Hernandez, F. C.; Priyadarshana, G.; Sandaruwan, C.; Yang, W.; Karunaratne, V.; Wang, Z.; Amaratunga, G. A. J.; Kottegoda, N.; Meiyazhagan, A.; Ajayan, P. M. Pseudobrookite based heterostructures for efficient electrocatalytic hydrogen evolution. *Materials Reports: Energy* **2021**, *1* (2), 100020.
(64) Wang, C.; Li, C.; Liu, J.; Guo, C. Engineering transition metal-based nanomaterials for high-performance electrocatalysis. *Materials Reports: Energy* **2021**, *1* (1), 100006.
(65) Liu, Y.; Liu, S.; Wang, Y.; Zhang, Q.; Gu, L.; Zhao, S.; Xu, D.; Li, Y.; Bao, J.; Dai, Z. Ru Modulation Effects in the Synthesis of

Unique Rod-like Ni@Ni2P−Ru Heterostructures and Their Remarkable Electrocatalytic Hydrogen Evolution Performance. *J. Am. Chem. Soc.* **2018**, *140* (8), 2731−2734.
(66) McCrory, C. C. L.; Jung, S.; Peters, J. C.; Jaramillo, T. F. Benchmarking Heterogeneous Electrocatalysts for the Oxygen Evolution Reaction. *J. Am. Chem. Soc.* **2013**, *135* (45), 16977−16987.
(67) Mei, B.-A.; Munteshari, O.; Lau, J.; Dunn, B.; Pilon, L. Physical Interpretations of Nyquist Plots for EDLC Electrodes and Devices. *J. Phys. Chem. C* **2018**, *122* (1), 194−206.
(68) Zhang, J.; Zhao, Y.; Guo, X.; Chen, C.; Dong, C.-L.; Liu, R.-S.; Han, C.-P.; Li, Y.; Gogotsi, Y.; Wang, G. Single platinum atoms immobilized on an MXene as an efficient catalyst for the hydrogen evolution reaction. *Nature Catalysis* **2018**, *1* (12), 985−992.

https://doi.org/10.1021/acsanm.2c01639
ACS Appl. Nano Mater. 2022, 5, 9319−9333